energies

MDPI

Article

Switched-Capacitor Boost Converter for Low Power Energy Harvesting Applications

Miran Rodič *, Miro Milanovič, Mitja Truntič and Benjamin Ošlaj

Faculty of Electrical Engineering and Computer Science, University of Maribor, Koroška Cesta 46, SI-2000 Maribor, Slovenia; miro.milanovic@um.si (M.M.); mitja.truntic@um.si (M.T.); benjamin.oslaj@um.si (B.O.)

* Correspondence: miran.rodic@um.si; Tel.: +386-2-220-7308

Received: 19 October 2018; Accepted: 13 November 2018; Published: 14 November 2018

Abstract: The paper presents a Switched-Capacitor Boost DC-DC Converter (SC-BC) which can be used in energy harvesting applications using thermoelectric generators (TEGs) with low output voltage, low power and a significant internal resistance. It consists of a switching capacitor circuit, where MOSFETs are used as switches, and a boost stage. The converter is a modification of a previously presented scheme in which diodes are used in the switched capacitor stage. A higher voltage gain and an increased efficiency can thus be achieved. The model of the converter was developed considering the internal resistance of the TEG and boost stage inductor. A comparison with the diode based converter is shown, with consideration of the TEG internal resistance. Calculation is presented of the main passive components. A control algorithm is also proposed and evaluated. It is based on a linearization approach, and designed for output voltage and inductor current control. The operation of both converter and control are verified with the simulation and experimental results.

Keywords: DC-DC converter; switched capacitor; high voltage gain; energy harvesting

1. Introduction

Photovoltaic (PV) systems suffer from temperature-related reduction of the produced power in the case of increased temperature of the panel surface. The current state-of-art in this field is to use passive cooling with a liquid coolant [1,2], but researchers have also focused on radiative cooling approaches [3,4]. An idea for the solution of this problem is to apply thermoelectric generators (TEGs) to the back of the panels and, thus, provide active cooling [5,6]. Furthermore, because the TEGs also produce energy due to the temperature difference between their surfaces, this effect can be used for cogeneration purposes, as energy harvesting [7,8]. Theamount of energy produced is relatively low when compared to that produced by the PV panels, but it is sufficient to allow an increase of the PV panel power production. The main problem when using low temperature TEGs is their low output voltage (a few volts), therefore, an appropriate DC-DC converter has to be used. In such a converter, all the applied diodes represent a significant voltage drop. Also, the TEG itself has a significant internal resistance (in the range of Ohms). These facts stimulated the researchers in the field to investigate different inverter structures with high voltage gains [9–11].

The classical solution would be to use a Continuous Conduction Mode or Discontinuous Conduction Mode (CCM/DCM) boundary operated boost converter, with few switching elements and, therefore, high efficiency and low losses [12]. The limitations of this structure occur due to the high internal resistance of the TEG, which limits the voltage gain of the converter. Additionally, when high voltage gain is required, the converter has to operate with either very low or very high duty cycles (down to 0.1 or up to 0.9), resulting in reduced efficiency and, in some cases, highly nonlinear behaviour. Another option would be to use the Luo-superlift converter [13,14]. However, the limitations of this

converter are also in the voltage gain limitations. Namely, to achieve a voltage gain in the range of 10 or higher, multiple stages would be required in the converter, which would result in a higher number of switching elements and decreased efficiency.

The use of transformers in the converter, as it is in the case with a flyback converter, would be another option [13]. With the appropriate transformer applied, high voltage gain could be achieved easily. The problem of using such converter would be due to the power dissipation on the leakage inductance of the transformer. Moreover, if the converter application does not require isolation, the cost, losses, mass and volume of the converter would increase significantly. Other candidates, switched-capacitor converters [15,16], operate with relatively low efficiency and introduce di/dt related problems into the circuit. Intuitively, putting two or more converters into cascade could also be an option. However, the losses of converters would add up, resulting in reduced efficiency of the system. So-called quadratic converters [17–20] can achieve the voltage gain of the cascaded converters with fewer switches, but voltage or current overstresses could be present. Finally, hybrid converters are becoming an interesting solution [21–25]. An interesting approach, combining switching-capacitor and boost converter, was presented in [26,27] (Figure 1). The converter is capable of achieving high voltage gain (in the range of 10). However, the problem with this converter is that a high number of diodes is applied, each of them introducing a significant voltage drop and, thus, a new structure replacing the diodes with the MOSFET transistors is proposed in this paper. The voltage gain of the converter is increased significantly when compared to the converter using diodes. The efficiency is improved, because the voltage drop on the transistors is smaller than the one on the diodes, and, in the switched capacitor circuit, the voltage drop in a diode based converter is on two diodes and one MOSFET, whereas in a MOSFET based converter, the voltage drop is on two MOSFETs. The same is true for the power losses. The improvements regarding the gain characteristics are demonstrated using analytical methods and experimental results in the form of the measurements' results. The modelling was done using a realistic TEG source model, where the internal resistance is significant. This means that the voltage drops on MOSFETs can be neglected, or presented as a part of the internal resistance of the source. Likewise, capacitors have a very small ESR (Equivalent Series Resistance), so it is much lower than the resistance of the TEG and load, and can be neglected. A control algorithm is proposed and evaluated. The linearization method was used, as presented in [28,29]. The model was first linearised, and afterwards controlled with the linear controller.

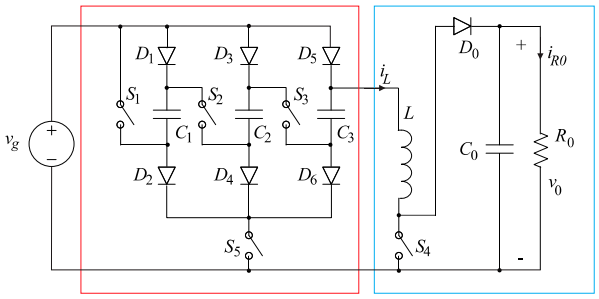

Figure 1. Switched capacitor-boost converter, basic principle; SC-circuit is represented in the red frame and BC in the blue frame.

The research focuses regarding the use of power electronics converters in the applications of energy harvesting are in the solving of problems of using the low power and output voltage devices (like TEGs) more efficiently with either a reduced number of elements, or by integration in dedicated Systems on Chip (SOC). Due to their high cost, volume and weight, the goal is to reduce the number of inductors, as well as their inductance, or to replace them with capacitors. In many cases, diodes are used as passive switching elements, which introduce a significant voltage drop into the circuit, resulting in significant conducting power losses. The problems connected with the high internal resistance of TEG are also addressed. In the field of development of DC-DC converters in such applications, the increasing of voltage

gain and efficiency are the main issues, because limits are set to them based on the converter setup and elements. For example, in several converter topologies the duty cycle can become very low or very high in the case when a high voltage gain is required. This can result in highly nonlinear, or even unstable, behaviour. The focus is also on the possibility of using lower voltage and current switches, as well as reducing the overall element count.

The main contributions of this paper are the improvement of an existing DC-DC converter scheme presented in [26,27], modelling of the converter, the derivation of the algorithm for choice of passive components, and the design of the model-based nonlinear control algorithm. The improvement of the converter is achieved by the replacement of the passive switching elements (diodes) with the active ones (MOSFETs), thereby reducing conduction losses significantly, which is represented in improved efficiency (95% at the maximum point compared to 79% in the case of the diode based converter). Additionally, the duty cycle is not overlong or overshort. The model of the converter was obtained using the state space averaging method, as presented in [30]. The model is used for the evaluation of static behaviour (voltage gain), choice of parameters for the passive elements (inductors and capacitors), and design of the control algorithms. Internal resistance of TEG is taken into account in the modelling of the system. The design and control are evaluated with simulations and experiments.

The paper is organised as follows: Section 1 gives an introduction of the PV system upgraded with the introduction of TEG for thermal energy harvesting. The need for the use of a high voltage gain DC-DC converter is presented, based on the problems occurring with the use of TEG. Several existing solutions are presented briefly, and a new Switched-Capacitor Boost DC-DC Converter (SC-BC) structure is introduced. The principle of the operation for this new structure is described in detail in Section 2, where modes of the operation are described. In Section 3, the modelling of SC-BC is presented. A state-space model was developed using the state averaging principle. The resulting dynamic model is represented with formulas and a block scheme. The gain characteristics of the converter are presented in Section 4. Choice of the SC-BC passive components is described in Section 5. The derivation and explanation of the control algorithm for SC-BC is done in Section 6. A model-based approach was used, applying the linearization principle. Results are presented in Section 7, where the verification of static characteristics and control algorithm with the simulation and experimental results are given. In Section 8, a discussion is presented regarding the results and findings.

2. Principle of Operation

Figure 1 shows the Switching-Capacitor-Boost Converter (SC-BC) introduced in [15]. The hybrid converter consists of two stages. The first stage is a Switching-Capacitor circuit (SC, red frame in Figure 1), which is responsible for multiplying the input voltage by the parallel-series interconnecting operation, and the second stage is the Boost Stage (BS, blue frame in Figure 1), further increasing the output voltage. In this scheme, the voltage source is supposed to be ideal. However, when it is applied for energy harvesting using TEG as an input, this voltage source has a significant inner resistance R_g (in the range of 1 Ω to 3 Ω). The diode voltage drops also result in significant reduction of the total converter voltage gain. The detailed scheme of this converter is shown in Figure 2a, where the internal resistance R_g is considered, and MOSFETs are applied as switches S_1 to S_5.

To reduce the voltage drop in the switching capacitor stage, the improved structure of SC-BC, where the diodes are replaced by MOSFETs, is presented in Figure 2b. The SC-BC operates in three modes. For the diode variant in the first sequence the switches T_4 and T_5 are switched on and T_1, T_2, and T_3 are switched off. The capacitors C_1, C_2 and C_3 are charged, and also the inductor current i_L starts charging the inductor L. The slope of inductor current is defined by converter input voltage v_{gg} (v_g is the open terminal TEG voltage) and inductance L. The voltages v_{C1}, v_{C2} and v_{C3} on the SC stage capacitors are rising. Capacitor voltage v_0 is discharged to the load R_0. i_{R0} is the output load current.

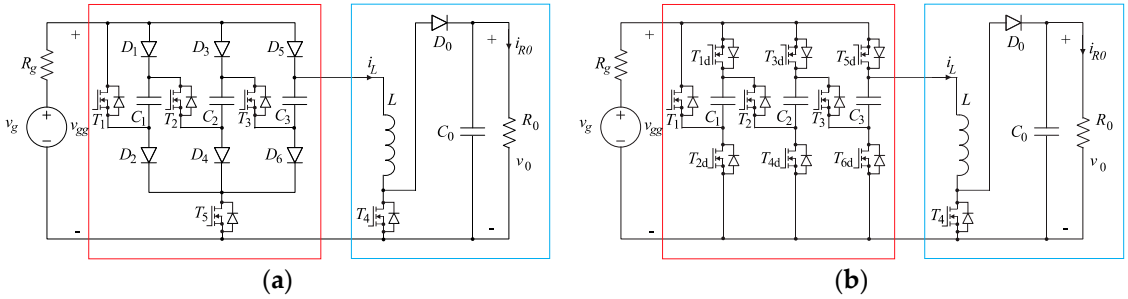

Figure 2. Switched Capacitor-Boost Converter (SC-BC), the SC-circuit is represented in the red frame and BC in the blue frame: (**a**) Diode based SC-BC; (**b**) MOSFET based SC-BC.

An equivalent circuit for this mode of operation is shown in Figure 3a. Voltage drops on diodes are represented by V_D. The same mode of operation is shown in Figure 3b for a MOSFET based converter, where the transistors T_{1d}, T_{2d}, T_{3d}, T_{4d}, T_{5d}, and T_{6d}, as well as switch T_4, are switched on, whereas the transistors T_1, T_2, and T_3 are switched off. In the second sequence for the diode circuit, T_5 is switched off and transistors T_1, T_2, T_3 and T_4 are switched on, and, for the MOSFET circuit, transistors T_{1d}, T_{2d}, T_{3d}, T_{4d}, T_{5d}, and T_{6d} are switched off, whereas the transistors T_1, T_2, T_3, and T_4 are switched on. The equivalent circuit is equal for diode and MOSFET based converters, and is shown in Figure 3c. In this mode, the voltages v_{gg}, v_{C1}, v_{C2} and v_{C3} are series connected and provide the higher voltage to the BS input, charging the inductor L with their sum. The slope of the inductor current increased as a consequence of higher input voltage in the boost converter stage. Capacitor voltage v_0 is, as in the first sequence, discharged to the load R_0. In the third sequence, transistors T_1, T_2 and T_3 are switched on in both converters, whereas the transistors T_4 and T_5 are switched off in the diode-based circuit, and the transistors T_4, T_{1d}, T_{2d}, T_{3d}, T_{4d}, T_{5d}, and T_{6d} are switched off in the MOSFET based circuit. The energy stored in inductor L, combined with the voltage source and the energy stored in capacitors C_1, C_2 and C_3, is pushed into the output capacitor C_0 and supports the output voltage v_0, at the same time, charging the load R_0.

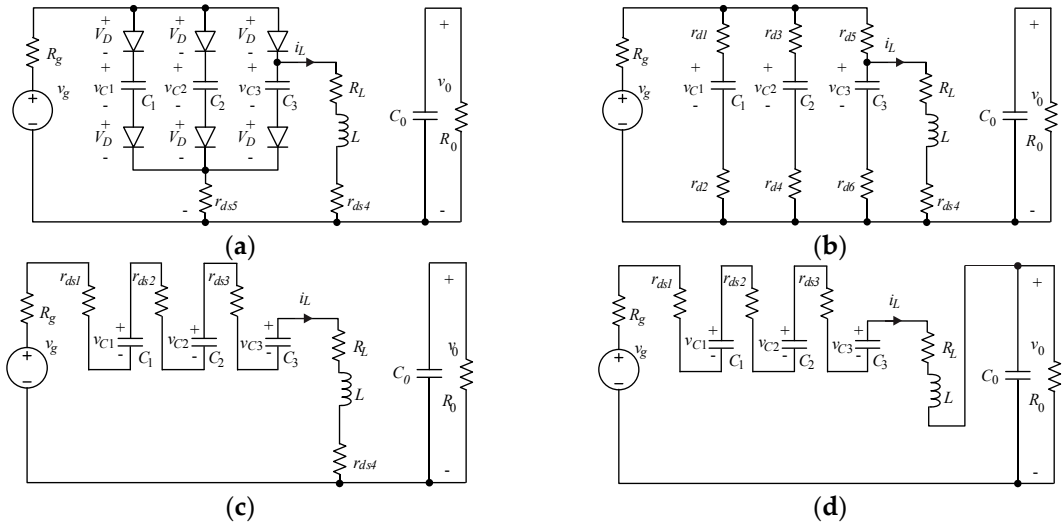

Figure 3. Switched-Capacitor-Boost Converter modes of operation: (**a**) Diode based converter, parallel charging of SC stage capacitors and inductor; (**b**) MOSFET based converter, parallel charging of SC stage capacitors and inductor; (**c**) Both variants, charging inductor from SC capacitors in series with voltage source; (**d**) Both variants, discharging to output.

An equivalent circuit for this mode of operation is shown in Figure 3d and is, as in the case of the second sequence, equal for diode and MOSFET based converters. The transistors in the circuit are represented by their resistances: r_{ds1} for T_1, r_{ds2} for T_2, r_{ds3} for T_3, r_{ds4} for T_4, r_{ds5} for T_5, r_{d1} for T_{1d}, r_{d2} for T_{2d}, r_{d3} for T_{3d}, r_{d4} for T_{4d}, r_{d5} for T_{5d}, and r_{d6} for T_{6d}. The same transistors are used for all of the switches; therefore, all the resistances are the same. The resistance of inductor L is represented by the resistance R_L.

Figure 4a,b shows the corresponding triggering signals, inductor current and voltage v_L in the SC-BC for diode and MOSFET based structures, respectively. The duration of the first sequence is zdT_s, where z is the switched capacitors' charging duty cycle over the interval dT_s, where d is the duty cycle function over the interval T_s ($T_s = 1/f_s$, where f_s is the switching frequency of the converter). The duration of the second sequence is $(1 - z)\, dT_s$, and the duration of the third sequence is $(1 - d)\, T_s$. The average values of z and d are represented with Z and D, respectively, and the average value of the inductor current i_L is represented by I_L.

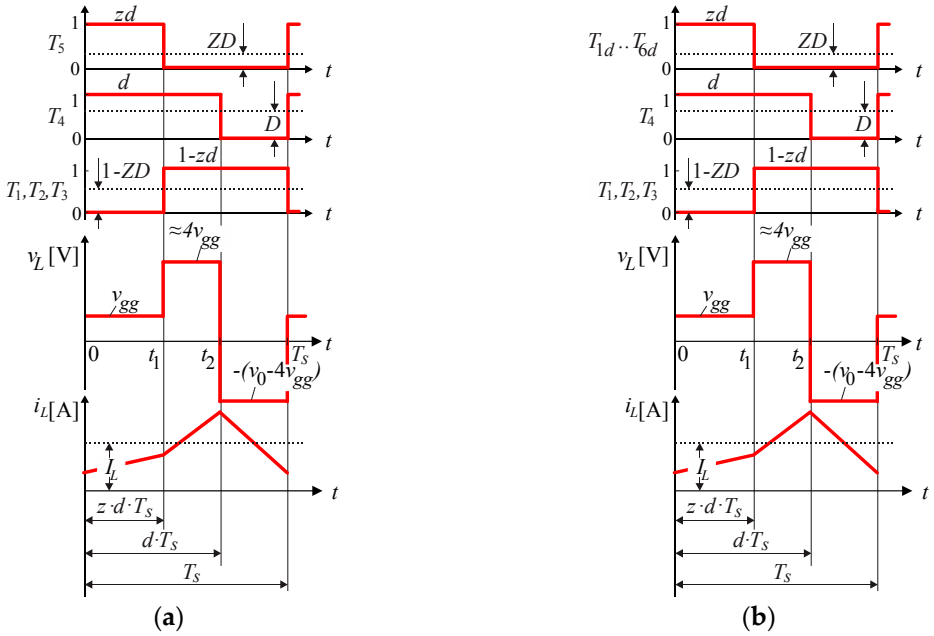

Figure 4. Switching sequences: (**a**) Diode based SC-BC; (**b**) MOSFET based SC-BC.

3. SC-BC Modelling

The state space averaging method was used in order to obtain the dynamic model and static characteristics of both converter structures. The Schottky diodes (VSSB420S-M3 with forward voltage $V_D = 0.8$ V) were chosen in the case of diode based converters. The voltage drop on the diode was significant compared to the one expected on the MOSFET on-resistance ($R_{DS(on)} = 10$ mΩ), indicated in the Figure 3a–d by $r_{d1} - r_{d6}$, $r_{ds1} - r_{ds5}$. The voltage drop on the $R_{DS(on)}$ (MOSFET drain-source on resistance) was evaluated as 2.5% of the voltage drop on the diodes and can be neglected, as well as the equivalent series resistances of capacitors. Equal values are used for capacitances of capacitors C_1, C_2 and C_3:

$$C_1 = C_2 = C_3 = C_k, \tag{1}$$

and, for both converters, it can be assumed that the three legs of the switched capacitor circuit are symmetrical, resulting in:

$$v_{C1} = v_{C2} = v_{C3} = v_{Ck} \tag{2}$$

Voltages v_{C1}, v_{C2}, and v_{C3} are, thus, replaced by the voltage v_{Ck} in the following text. In order to perform mathematical analysis of SC-BC for static analyses (gain calculation) and controller parameter design, the dynamic model needs to be derived for diode and MOSFET-based converters.

3.1. Mathematical Analysis of Diode Based SC-BC

The SC-BC [26,27] operates in three sequences, represented in the Figures 3 and 4. In the first sequence, with the duration of zdT_s (Figure 4a), the switches T_4 and T_5 are switched on and T_1, T_2, and T_3 are switched off. The model, described by state variables v_{Ck}, i_L and v_0 and using an equivalent circuit, presented in Figure 3a, can be written as:

$$\begin{aligned} \frac{dv_{Ck}}{dt} &= -\frac{1}{3R_gC_k}v_{Ck} - \frac{1}{3C_k}i_L + \frac{1}{3R_gC_k}(v_g - 2v_D), \\ \frac{di_L}{dt} &= \frac{1}{L}(v_{Ck} + v_D) - \frac{R_L}{L}i_L, \\ \frac{dv_0}{dt} &= -\frac{1}{R_0C_0}v_0. \end{aligned} \tag{3}$$

In the second sequence, (with the duration of $(1 - z)dT_s$, Figure 4a), T_5 is switched off and transistors T_1, T_2, T_3 and T_4 are switched on. The equivalent circuit is shown in Figure 3c, and its model is represented as follows:

$$\begin{aligned} \frac{dv_{Ck}}{dt} &= -\frac{1}{C_k}i_L, \\ \frac{di_L}{dt} &= \frac{3}{L}v_{Ck} - \frac{R_g+R_L}{L}i_L + \frac{1}{L}v_g, \\ \frac{dv_0}{dt} &= -\frac{1}{R_0C_0}v_0. \end{aligned} \tag{4}$$

In the third sequence, transistors T_1, T_2 and T_3 (with the duration of $(1 - d)T_s$, Figure 4a), are switched on, and the transistors T_4 and T_5 are switched off, and, with the help of the equivalent circuit shown in Figure 3d, the dynamic model representing this operation mode can be written as:

$$\begin{aligned} \frac{dv_{Ck}}{dt} &= -\frac{1}{C_k}i_L, \\ \frac{di_L}{dt} &= \frac{3}{L}v_{Ck} - \frac{R_g+R_L}{L}i_L - \frac{1}{L}v_0 + \frac{1}{L}v_g, \\ \frac{dv_0}{dt} &= \frac{1}{C_0}i_L - \frac{1}{R_0C_0}v_0. \end{aligned} \tag{5}$$

Equation (3) describes the trajectory of state variables in time interval $t \in (0, t_1)$, Equation (4) in interval $t \in (t_1, t_2)$ and Equation (5) in interval $t \in (t_2, T_S)$. According the notation indicated in Figure 4, the variables z and d (duty-cycle signals) are defined as follows:

$$zd = \begin{cases} 1, & 0 \le t < t_1 \\ 0, & t_1 \le t \le T_S \end{cases}$$
and
$$d = \begin{cases} 1, & 0 \le t < t_2 \\ 0, & t_2 \le t \le T_S \end{cases} . \tag{6}$$

To obtain the state space average model, Equations (3)–(5) are multiplied with the duty-cycle signals' combination zd, $(1 - z)d$ and $(1 - d)$, respectively. Finally, its sum represents a model of SC-BC as follows:

$$\begin{aligned} \frac{dv_{Ck}}{dt} &= -\frac{1}{3R_gC_k}v_{Ck}zd - \frac{1}{C_k}i_L\left(1 - \frac{2zd}{3}\right) + \frac{1}{3R_gC_k}v_gzd - \frac{2}{3R_gC_k}v_Dzd, \\ \frac{di_L}{dt} &= \frac{1}{L}v_{Ck}(3 - 2zd) - \frac{R_L+R_g(1-zd)}{L}i_L - \frac{1}{L}v_0(1 - d) + \frac{1}{L}v_g(1 - zd) + \frac{1}{L}v_Dzd, \\ \frac{dv_0}{dt} &= \frac{1}{C_0}i_L(1 - d) - \frac{1}{R_0C_0}v_0. \end{aligned} \tag{7}$$

According to the state space averaging modelling principle, the operation of the converter must be considered by introducing of small signal perturbation in the vicinity of the operating point. So, all state space variables (v_{Ck}, i_L, v_0), input voltage (v_g) and control variables (zd, d) from Equation (7) must be described in the form of $x = X + \widetilde{x}$, where X represents the average value of x, and $\widetilde{x}$ represents the small signal perturbation. In order to develop the model and ignoring small signal perturbations, only the average values of state space variables shall be considered, like:

$$V_{Ck} = \frac{1}{T_S}\int_0^{T_S} v_{Ck}dt; \quad \text{so it follows } v_{Ck} \Rightarrow V_{Ck}. \tag{8}$$

Consequently, other system variables shall also be indicated only by steady state operating points, expressed by capital letters:

$$i_L \Rightarrow I_L;\ v_0 \Rightarrow V_0;\ v_g \Rightarrow V_g;\ v_D \Rightarrow V_D;\ d \Rightarrow D; zd \Rightarrow ZD. \tag{9}$$

Thus, by substituting Equations (8) and (9) into Equation (7), the large-signal non-linear dynamic model is obtained, as follows:

$$\begin{aligned} \tfrac{dV_{Ck}}{dt} &= -\tfrac{1}{3R_gC_k}V_{Ck}ZD - \tfrac{1}{C_k}I_L\left(1-\tfrac{2ZD}{3}\right) + \tfrac{1}{3R_gC_k}V_gZD - \tfrac{2}{3R_gC_k}V_DZD, \\ \tfrac{dI_L}{dt} &= \tfrac{1}{L}V_{Ck}(3-2ZD) - \tfrac{R_L+R_g(1-ZD)}{L}I_L - \tfrac{1}{L}V_0(1-D) + \tfrac{1}{L}V_g(1-ZD) + \tfrac{1}{L}V_DZD, \\ \tfrac{dV_0}{dt} &= \tfrac{1}{C_0}I_L(1-D) - \tfrac{1}{R_0C_0}V_0. \end{aligned} \tag{10}$$

3.2. Mathematical Analysis of MOSFET Based SC-BC

The same procedure as is described in Section 3.1 can be used to obtain the MOSFET-based SC-BC model. The diodes are replaced by MOSFETs and, in the first sequence, with the duration of zdT_s (Figure 4b), the transistors T_{1d}, T_{2d}, T_{3d}, T_{4d}, T_{5d}, and T_{6d}, as well as switch T_4 are switched on, whereas the transistors T_1, T_2, and T_3 are switched off. Repeating the whole procedure from the previous subsection (described in Equations (3) to (10)) and replacing the model in Equation (3) of the first sequence with:

$$\begin{aligned} \tfrac{dv_{Ck}}{dt} &= -\tfrac{1}{3R_gC_k}v_{Ck} - \tfrac{1}{3C_k}i_L + \tfrac{1}{3R_gC_k}v_g, \\ \tfrac{di_L}{dt} &= \tfrac{1}{L}v_{Ck} - \tfrac{R_L}{L}i_L, \\ \tfrac{dv_0}{dt} &= -\tfrac{1}{R_0C_0}v_0, \end{aligned} \tag{11}$$

An average model of the MOSFET based SC-BC can be expressed by:

$$\frac{dV_{Ck}}{dt} = -\frac{1}{3R_gC_k}V_{Ck}ZD - \frac{1}{C_k}I_L\left(1-\frac{2ZD}{3}\right) + \frac{1}{3R_gC_k}V_gZD, \tag{12}$$

$$\frac{dI_L}{dt} = \frac{1}{L}V_{Ck}(3-2ZD) - \frac{R_L+R_g(1-ZD)}{L}I_L - \frac{1}{L}V_0(1-D) + \frac{1}{L}V_g(1-ZD), \tag{13}$$

$$\frac{dV_0}{dt} = \frac{1}{C_0}I_L(1-D) - \frac{1}{R_0C_0}V_0. \tag{14}$$

For the MOSFET based SC-BC, a block scheme of the dynamic model is featured in Figure 5. Using Equations (12)–(14), it is possible to obtain the SC-BC gain characteristics, and also the dynamic model necessary to establish and design the control algorithms for the SC-BC inductor current I_L and output voltage V_0.

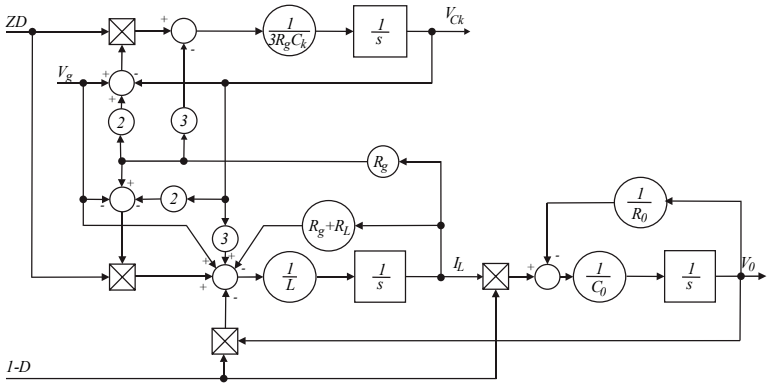

Figure 5. Dynamic model of the MOSFET based SC-BC.

4. SC-BC Gain Characteristics

Considering Equation (10) during the steady state, all derivatives fulfil the condition:

$$\frac{dV_{Ck}}{dt} = 0, \ \frac{dI_L}{dt} = 0 \ \text{and} \ \frac{dV_0}{dt} = 0, \tag{15}$$

The steady state value of the output voltage V_0 can be evaluated for a diode based circuit from Equation (10) as is described in [26,27]:

$$\begin{aligned} V_0 \ &= \frac{(1-D)ZD(4-3ZD)R_0}{ZDR_L+\left(9-11ZD+3(ZD)^2\right)R_g+(1-D)^2ZDR_0}V_g \\ &- \frac{(1-D)ZD(6-5ZD)R_0}{ZDR_L+\left(9-11ZD+3(ZD)^2\right)R_g+(1-D)^2ZDR_0}V_D \end{aligned}, \tag{16}$$

where V_g and V_D represent the average value of the open terminal TEG voltage v_g and average value of the diode forward voltage v_D respectively. ZD and D represent the average values of zd and d, within the interval T_s respectively, as shown in Figure 4a,b.

In the case of the MOSFET based SC-BC, the average value of the output voltage can be calculated from Equations (12)–(14) in the steady state operation (described by Equation (15)) using the same approach as presented for diode based SC-BC:

$$V_0 = \frac{(1-D)ZD(4-3ZD)R_0}{ZDR_L+\left(9-11ZD+3(ZD)^2\right)R_g+(1-D)^2ZDR_0}V_g. \tag{17}$$

When the result is compared to Equation (16) it can be observed that the only difference is in the absence of the second term, multiplied by the diode voltage drop V_D. Based on Equations (16) and (17), the 3D-diagram is calculated and plotted by using MATLAB (v2015b, Mathworks, Natick, MA, USA). Figure 6a,b shows the calculated output voltage for diode and MOSFET based SC-BC respectively. It is evident that the MOSFET based SC-BC produces the higher output voltage, which is indicated in the chosen operational points D = 0.6 and ZD = 0.4. When observing Figures 6 and 7 it shall be noted that they represent the calculated values and, in the real operation, the duty cycle D cannot be lower than ZD.

The converter static gain characteristics A_v, representing the voltage gain regarding the converter input voltage, are obtained by neglecting the TEG inner resistance in Equation (17) by setting $R_g \rightarrow 0$ as follows:

$$A_v = \frac{V_0}{V_{gg}} = \frac{(1-D)(4-3ZD)R_0}{R_L+(1-D)^2R_0}, \tag{18}$$

where V_{gg} is the SC-BC input terminal voltage, and is calculated as:

$$V_{gg} = V_g - I_{in}R_g. \tag{19}$$

I_{in} is the SC-BC converter average input current. Figure 7a,b shows the changing of the input terminal voltage, which depends on all converter resistances and their operating points (R_g = 1 Ω, R_0 = 70 Ω, and R_L = 75 mΩ), and the SC-BC gain characteristic, respectively.

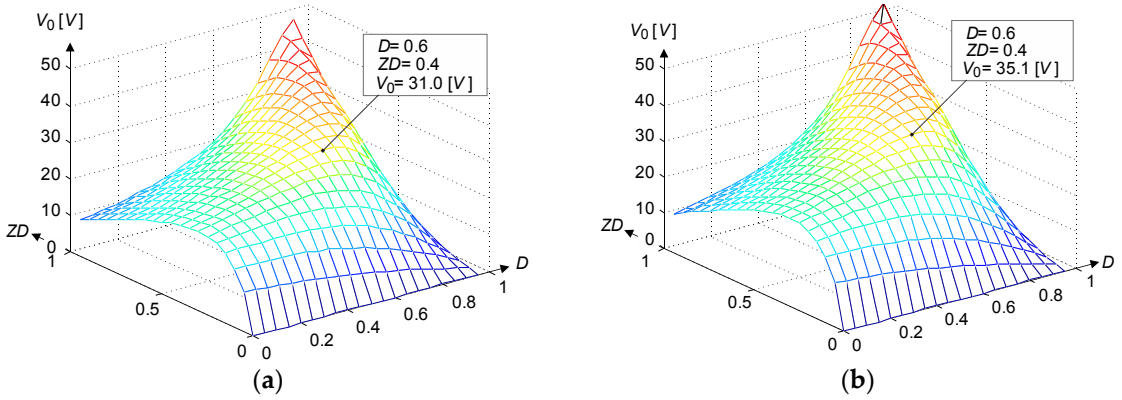

Figure 6. Calculated output voltages of SC-BC: (**a**) For diode based circuit $V_0 = f(D,ZD)$ (V_g = 8.6 V, V_D = 0.8 V); (**b**) For MOSFET based circuit $V_0 = f(D,ZD)$ (V_g = 8.6 V, V_D = 0.0 *V*).

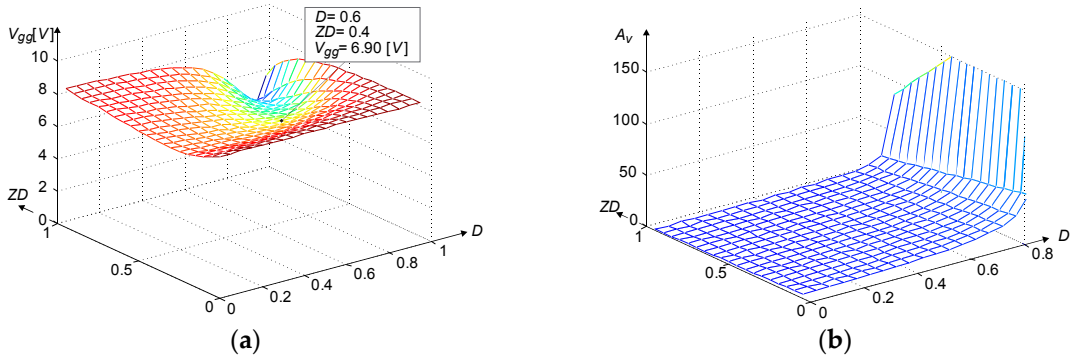

Figure 7. SC-BC operation: (**a**) Calculated input terminal voltages of SC-BC; (**b**) Calculated gain characteristics for MOSFET based circuit $A_v = f(D,ZD)$; where V_D = 0.

Maximal output voltage is calculated from the derivative of Equation (17), when it is rewritten to the following form:

$$\frac{V_0}{V_g} = \frac{(1-D)ZD(4-3ZD)R_0}{ZDR_L + \left(9-11ZD+3(ZD)^2\right)R_g + (1-D)^2 ZDR_0}. \tag{20}$$

The value of the product ZD is considered constant, and the maximal value will be achieved for the duty cycle D, for which it is possible to claim:

$$\frac{\partial\left(\frac{V_0}{V_g}\right)}{\partial D} = 0. \tag{21}$$

The solution of this equation is:

$$D_{\max} = 1 - \frac{\sqrt{ZDR_0\left(ZDR_L + \left(9-11ZD+3(ZD)^2\right)R_g\right)}}{ZDR_0}, \tag{22}$$

which is the maximal value of D. The minimal value of the duty cycle is set by the choice of ZD, because Z can not be lower than 1:

$$D_{\min} = ZD. \tag{23}$$

The maximal and minimal values of the available output voltage V_0 can, thus, be calculated if D_{max} and D_{min} are introduced into the Equation (20)). These values have to be applied as the dynamic limits (dependent on the chosen ZD) of the control algorithm output in order to ensure the stability of operation.

5. Choice of SC-BC Passive Elements

The main passive elements, as are inductor L, capacitors C_0 and C_k, in the SC-BC need to be chosen based on the requirements set to the SC-BC circuit. Figure 8 shows ideal waveforms of the necessary inductor current i_L and output voltage v_0, together with the inductor voltage v_L and the current i_{D0} passing the diode D_0.

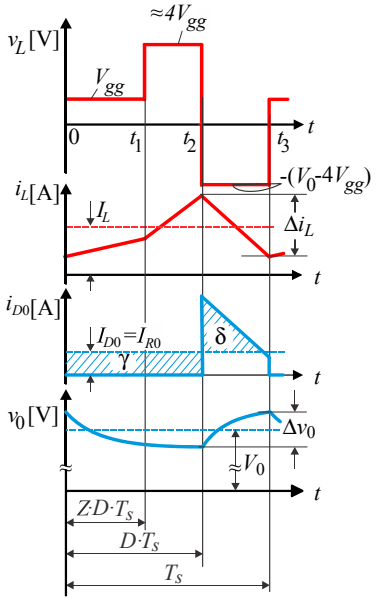

Figure 8. Switching sequences for current and voltage ripple, necessary for design of passive elements.

The procedure for the choice of inductor and output capacitor is based on the approach described in [30], utilising the inductor current and output voltage ripple. When steady state of the SC-BC operation is achieved, the inductor current ripple can be evaluated by observing the inductor current curve in time interval $t \in (t_2, t_3)$, as indicated in Figure 8:

$$i_L(t) = i_L(t_2) - \frac{V_0 - 4V_{gg}}{L}(t - t_2). \tag{24}$$

Regarding the current waveform, it can be noted that $i_L(t_2) = I_{L,max}$ and $i_L(t_3) = I_{L,min}$, therefore the current ripple is defined as:

$$\Delta i_L = I_{L,\min} - I_{L,\max} = -\frac{V_0 - 4V_{gg}}{L}(t_3 - t_2) \Rightarrow \Delta i_L = \frac{V_0 - 4V_{gg}}{L}(1 - D)T_s, \tag{25}$$

where the time interval is calculated as $t_3 - t_2 = (1 - D)T_s$. By dividing both sides of Equation (25) by I_L, it can be rewritten as:

$$\frac{\Delta i_L}{I_L} = -\frac{V_0 - 4V_{gg}}{LI_L}(1 - D)T_s, \tag{26}$$

Using the power balance (the input of BC stage of SC-BC is ideally equal to the output of SC-BC), the following is obtained:

$$V_{gg}^{*} I_L = V_0 I_0, \quad I_0 = \frac{V_0}{R_0} \quad \Rightarrow \quad I_L = \frac{V_0^2}{R_0 V_{gg}^{*}}, \tag{27}$$

where V_{gg}^{*} is the input of the boost stage of SC-BC, which, under the assumption that $V_{gg} \approx V_{Ck}$, can be rewritten in the following form:

$$V_{gg}^{*} = V_{gg} ZD + \left(V_{gg} + 3V_{Ck}\right)(1 - ZD) \approx (4 - 3ZD) V_{gg}. \tag{28}$$

Equation (28) is introduced to Equation (27):

$$I_L = \frac{V_0^2}{R_0 (4 - 3ZD) V_{gg}}, \tag{29}$$

and Equation (26) is rewritten as:

$$\frac{\Delta i_L}{I_L} = \frac{V_0 - 4V_{gg}}{L V_0^2} (1 - D)(4 - 3ZD) V_{gg} R_0 T_s, \tag{30}$$

from which the following inequity can be derived:

$$L \geq \frac{\left(V_0 - 4V_{gg}\right)(1 - D)(4 - 3ZD) V_{gg} R_0 T_s}{\frac{\Delta i_L}{I_L} V_0^2}. \tag{31}$$

According to the inductor current ripple (40%), choice of operation point and uncertainty of the parameters: $V_0 = 32$ V, $V_{gg} \in (6\,\text{V}, 8.6\,\text{V})$, $R_0 \in (55\,\Omega, 100\,\Omega)$, $Z = 0.6$, $D = 0.6$ and $T_s = 10$ µs (switching frequency is $f_s = 100$ kHz), the following inequity is used to choose the inductance:

$$L \geq 272\,\mu\text{H}.$$

For further consideration the value $L = 330$ µH was chosen.

As also follows from [30], the capacitance C_0 value can be chosen using the voltage waveforms featured in Figure 8 by blue colour. The area described by γ represents the charge Δq, which discharges the capacitor C_0 from $v_0(0) = v_{0,max}$ to $v_0(t_1) = v_{0,min}$. During this time, the capacitor C_0 is discharged with the current I_{R0}. The voltage ripple can be calculated as follows:

$$\Delta v_0 = V_{0,max} - V_{0,min} = \frac{\Delta q}{C_0} = \frac{I_{R0} D T_s}{C_0} = \frac{V_0}{R_0 C_0} D T_s, \tag{32}$$

which can be rewritten to represent the output voltage ripple:

$$\Delta v_0 = \frac{V_0}{R_0 C_0} D T_s \Rightarrow \frac{\Delta v_0}{V_0} = \frac{D T_s}{R_0 C_0}. \tag{33}$$

After rearrangement of Equation (33) the inequality for the choice of capacitor can be presented:

$$C_0 \geq \frac{D T_s}{R_0 \left(\frac{\Delta v_0}{V_0}\right)}. \tag{34}$$

Using the obtained inequality in Equation (34) the capacitance was evaluated to be (for $\Delta v_0 = 2\%$):

$$C_0 \geq 22\,\mu\text{F}.$$

For further analyses the C_0 = 40 µF was chosen.

The energy approach was used for the calculation of C_k. The main idea of this approach is that the inductor receives from the SC capacitors the difference in energy required for its charging.

$$W_L = W_{Ck} \Rightarrow 3\frac{C_k V_{Ck}^2}{2} = \frac{L\left(I_{L,max}^2 - I_{L,min}^2\right)}{2}. \tag{35}$$

Taking into account the assumption that $V_{gg} \approx V_{Ck}$, the following equation is derived:

$$3C_k V_{gg}^2 = L\left(I_{L,max}^2 - I_{L,min}^2\right), \tag{36}$$

which can be rewritten as:

$$3C_k V_{gg}^2 = L(I_{L,max} + I_{L,min})(I_{L,max} - I_{L,min}), \tag{37}$$

where the sum of maximal and minimal inductor current values is represented with the average inductor current value, and the difference of these two values represents the inductor current ripple:

$$I_L = \frac{1}{2}(I_{L,max} + I_{L,min}), \quad \Delta i_L = I_{L,max} - I_{L,min}. \tag{38}$$

Equation (37) can now be represented as:

$$3C_k V_{gg}^2 = 2L I_L \Delta i_L \tag{39}$$

and the capacitance C_k can be chosen on the basis of the following inequity:

$$C_k = \frac{2L I_L \Delta i_L}{3V_{gg}^2}. \tag{40}$$

The capacitance C_k was, thus, evaluated to be:

$$C_k \geq 19\ \mu\text{F}.$$

For further analyses the value C_k = 20 µF was chosen.

6. Control Algorithm

The control algorithm was developed for the MOSFET-based converter. A cascade control structure can be used for the control of the SC-BC, as presented in Figure 9a. The inductor current I_L is controlled in the inner loop, and the output voltage V_0 is controlled in the outer loop. The desired output voltage V_0^d is set by the user or the supervising system, whereas the desired value of the inductor current I_L^d is provided as an output of the voltage controller G_{v0}. The output of the inductor current controller G_{iL} is the duty cycle D. In some cases, when only the current control is required, as is the case when the TEG-powered power harvesting system is connected in parallel to another power source (for example a PV source), the inductor current control can be sufficient. Switched capacitor circuit voltages V_{Ck} can be controlled separately, almost independently from the aforementioned control; the output of the control is ZD, the switched capacitor charging duty cycle Z, multiplied by the duty cycle D, but the product can be applied as a separate variable, and it is only important to assure that the duty cycle D is not too small, i.e., lower than ZD, which can be achieved by setting of the controller limits (described in Equations (22) and (23)).

It would only be required to measure one of the switched capacitors circuit voltages, because the symmetry of the legs is provided by the adequate design. However, the measurement can be a cost issue and not practical (based on findings in [26] control of v_{Ck} could even result in reduced efficiency),

so the value of ZD can be set as a constant, as is the case for further simulation and experimental verification of the algorithms. In this case, the control scheme is featured in Figure 9b. The control algorithm of the SC-BC was developed using the linearization method as presented in [28,29]. It was developed on the base of the derived system model in Equations (12)–(14).

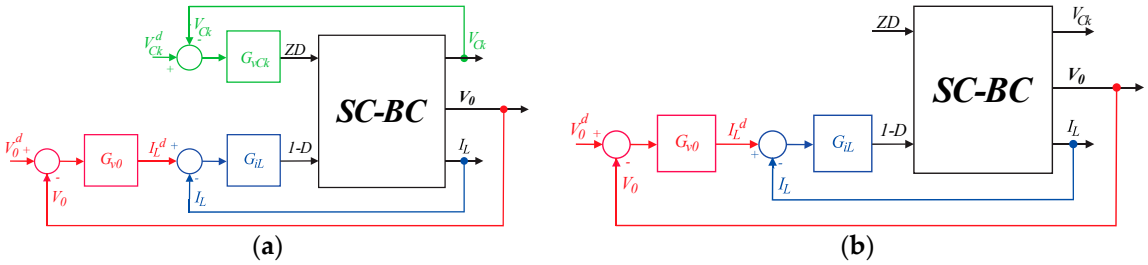

(**a**) (**b**)

Figure 9. Control scheme: (**a**) Basic principle of the SC-BC control; (**b**) Basic principle of the SC-BC control when constant value of ZD is used.

6.1. Control of Inductor Current I_L

The model of the inductor current in Equation (13) can be rewritten as:

$$L\frac{dI_L}{dt} + (R_L + R_g)I_L = V_g(1 - ZD) + V_{Ck}(3 - 2ZD) + R_g ZDI_L - V_0(1 - D). \tag{41}$$

The dynamic behaviour of the inductor current is highly nonlinear, and the use of a simple linear controller (for example a PI controller) would not be sufficient to assure a sufficiently precise and robust control. The solution of this problem is to linearise the nonlinear model in Equation (41) and apply the linear controller to the linearised model. In the first step it can be assumed that voltages on the capacitors C_k do not differ much from the converter input voltage $V_{gg}\cdot(V_{Ck} \approx V_{gg})$, thus Equation (41) can be rewritten as:

$$L\frac{dI_L}{dt} + (R_L + R_g)I_L = V_g(1 - ZD) + V_{gg}(3 - 2ZD) + R_g ZDI_L - V_0(1 - D). \tag{42}$$

The value of the duty cycle can now be calculated from:

$$1 - D = -\frac{1}{V_0}(U_{iL} - (\hat{V}_g(1 - ZD) + V_{gg}(3 - 2ZD) + \hat{R}_g ZDI_L)), \tag{43}$$

where $\hat{}$ represents the estimated values, $\hat{V}_g$ is the estimated value of the open terminal TEG voltage, and $\hat{R}_g$ the estimated value of the inner TEG resistance. U_{iL} represents the control variable, and is defined as an output of the PI controller, which will be used as the abovementioned linear controller. If it is assumed that TEG parameters are well known ($\hat{V}_g = V_g$ and $\hat{R}_g = R_g$) and the SC capacitor voltage equals the TEG terminal voltage ($V_{Ck} = V_{gg}$), the model in Equation (41) can be represented as a linear system:

$$L\frac{dI_L}{dt} + (R_L + R_g)I_L = U_{iL}, \tag{44}$$

which, as a result, gives the following transfer function to be controlled by the linear PI controller:

$$\frac{I_L(s)}{U_{iL}(s)} = \frac{1}{sL + (R_L + R_g)}, \tag{45}$$

where $U_{iL}(s)$ and $I_L(s)$ are Laplace transforms of the U_{iL} and I_L, respectively.

A block scheme is featured in Figure 10, where the controlled system is depicted in black, and the control algorithm in red colour. In order to perform the control algorithm, it is necessary to measure converter input and output voltage V_{gg} and V_0, respectively, and inductor current I_L.

The PI controller for the inductor current control is represented with the following transfer function:

$$\frac{U_{iL}(s)}{I_L^d(s) - I_L(s)} = K_{piL}\frac{1 + sT_{iiL}}{sT_{iiL}}, \tag{46}$$

where K_{piL} is the controller gain, and T_{iiL} the controller time constant. $I_L^d(s)$ is the Laplace transform of I_L^d. The design of the controller, i.e., calculation of the parameters (the chosen values were $K_{piL} = 0.5$ and $T_{iiL} = 55$ µs), is straightforward, and will not be described here. It is performed based on the assumption that the control plant is represented by Equation (44), and is thus represented by the transfer function in Equation (45).

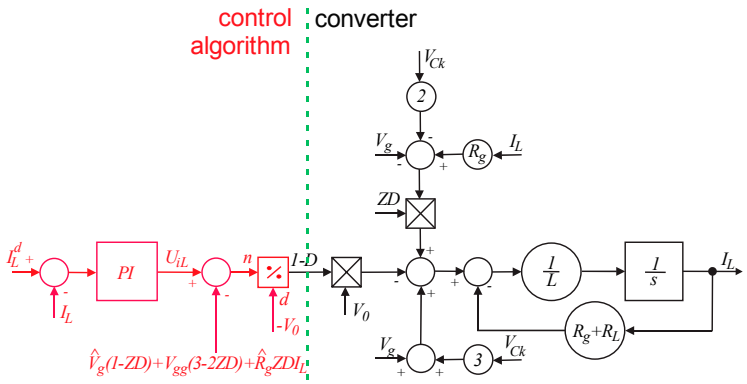

Figure 10. Control of inductor current—block scheme (converter model—black; control algorithm—red).

The variation of TEG parameters, open terminal voltage V_g and internal resistance R_g can be described as additive disturbance δ_{iL} in the control loop. If taken into consideration, Equation (44) has the following form:

$$L\frac{dI_L}{dt} + (R_L + R_g)I_L = U_{iL} + \delta_{iL}, \tag{47}$$

where the disturbance can be represented using Equations (41) and (42):

$$\delta_{iL} = (V_g - \hat{V}_g)(1 - ZD) + (V_{Ck} - V_{gg})(3 - 2ZD) + (R_g - \hat{R}_g)ZDI_L. \tag{48}$$

It is assumed that the TEG terminal voltage and SC capacitor voltage have almost the same value and the value of duty cycle ZD is known. TEG terminal voltage and inductor current are measured with sufficient precision. Thus, it can be observed that the value of disturbance is small, and, therefore, it should not present a problem. The behaviour of the control algorithm in the case of its presence can be described with the transfer function showing the disturbance rejection performed by the PI controller:

$$\frac{U_{iL}(s)}{\delta_{iL}(s)} = \frac{sT_{iiL}}{s^2L + s(R_g + R_L + K_{piL}T_{iiL}) + K_{piL}}, \tag{49}$$

from which it is obvious that the disturbance due to the TEG parameter variations will be completely rejected in a finite time.

6.2. Control of Output Voltage V_0

The control scheme for the output voltage is derived using the same methodology as the one for the inductor current control. The nonlinear model represented by Equation (14) is first linearised, and, in the second step, the linear controller is applied as a feedback controller of the linearised model.

The model of the output voltage in Equation (14) can be rewritten as:

$$R_0C_0\frac{dV_0}{dt} + V_0 = R_0I_L(1 - D). \tag{50}$$

Based on the ideal voltage gain value represented in Equation (18), where R_L is neglected, the value of the duty cycle $(1 - D)$ can be substituted as follows:

$$(1 - D) = \frac{(4 - 3ZD)V_{gg}}{V_0} \tag{51}$$

and Equation (50) can be rewritten as:

$$R_0 C_0 \frac{dV_0}{dt} + V_0 = \frac{(4 - 3ZD)V_{gg}}{V_0} R_0 I_L^d. \tag{52}$$

The model in Equation (52) remains nonlinear, and linearization is performed by applying the inverse function of idealised voltage gain (Equation (51)) to its input, deriving the desired value of inductor current using the following formula:

$$I_L^d = \frac{V_0}{(4 - 3ZD)V_{gg}\hat{R}_0} U_{v0}, \tag{53}$$

where $\hat{R}_0$ represents the estimated value of the load resistance, and U_{v0} is the control variable representing the output of the linear controller to be used as a feedback controller. The model presented in Equation (50) can now be rewritten as:

$$R_0 C_0 \frac{dV_0}{dt} + V_0 = U_{v0}, \tag{54}$$

The transfer function of the linearised system can now be represented as:

$$\frac{V_0}{U_{v0}} = \frac{1}{sR_0C_0 + 1}, \tag{55}$$

where $U_{v0}(s)$ and $V_0(s)$ are Laplace transforms of the U_{v0} and V_0, respectively. Graphical representation is featured in Figure 11, where the control algorithm is depicted in red and the controlled system in black.

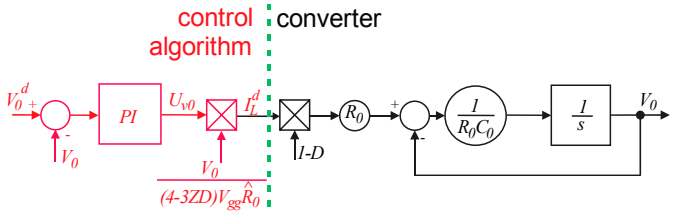

Figure 11. Control of output voltage—block scheme (converter model—black; control algorithm—red).

The PI controller is represented with the following transfer function:

$$\frac{U_{v0}(s)}{V_0^d(s) - V_0(s)} = K_{pv0}\frac{1 + sT_{iv0}}{sT_{iv0}}, \tag{56}$$

where K_{pv0} is the controller gain and T_{iv0} the controller time constant. V_0^d is the Laplace transform of the V_0^d. The design of the controller, i.e., calculation of the parameters (in the presented case the values K_{pv0} = 3.2, T_{iv0} = 4.8 ms were chosen), is again straightforward, and will not be described here. It was performed based on the assumption that the control plant is represented by Equation (54) and its transfer function is represented by Equation (55). A detailed block scheme of the complete control is given in Figure 12.

The variation of TEG parameters, open terminal voltage V_g and internal resistance R_g in this case have no obvious impact on the control behaviour. Taking into account Equations (18) and (53), and neglecting the internal resistance of the inductor, Equation (52) can be rewritten as:

$$R_0 C_0 \frac{dV_0}{dt} + V_0 = \frac{R_0}{\hat{R}_0} U_{v0}. \tag{57}$$

It can be observed that the load resistance R_0 is the main parameter with an impact on the precision. The input-output behaviour of the output voltage control loop can be represented by the following transfer function:

$$\frac{V_0(s)}{V_0^d(s)} = \frac{sT_{iv0} + 1}{s^2 T_{iv0} R_0 C_0 \frac{\hat{R}_0}{R_0 K_{pv0}} + s\left(T_{iv0} + T_{iv0} \frac{\hat{R}_0}{R_0 K_{pv0}}\right) + 1}. \tag{58}$$

Based on the transfer Equation (58) it can be assumed that the control behaviour should remain stable, even in the case of a significant variation of load resistance, if the PI controller gain K_{pv0} is chosen to perform a slightly more conservative control, i.e., its value is not set to the upper available limit. The precision of the control is achieved, because no static error will occur.

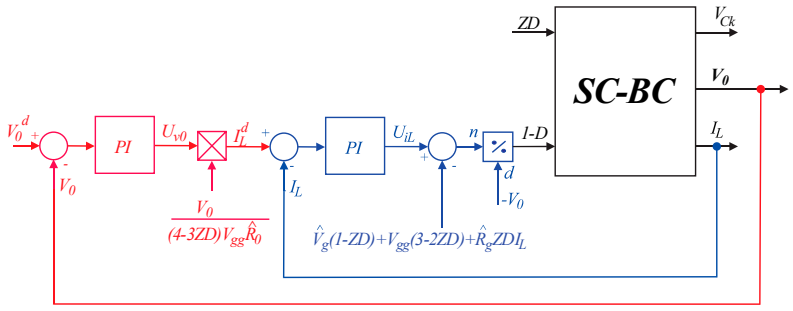

Figure 12. Control scheme—detailed graphical representation; constant value of *ZD* is used.

7. Results

A 30 W experimental prototype of the proposed MOSFET-based SC-BC was built, and the experimental results were carried out to prove the performed analysis of the static and dynamic behaviour of the converter. The experimental setup of the SC-BC is shown in Figure 13 with N-type MOSFETs (FDS5672) and appropriate passive components. In the experimental system the following values were chosen for the SC-BC parameters: L = 330 µH, R_L= 75 mΩ, C_k = 20 µF and C_0 = 40 µF. The basic value of load was set to R_0 = 60–100 Ω. The TEG parameters were V_g = 8.6 V, R_g = 1 Ω. Based on the state space averaging method, the converter gain characteristics were investigated, and, using the same approach, also the control algorithm, based on the non-linear compensation, was investigated. The results presented in this paper focus only on the SC-BC; the behaviour of the TEG is not evaluated. The TEG parameters are considered in the control design and in the evaluation of the parameter variation related disturbance rejection.

7.1. Verification of Gain Characteristics

The SC-BC gain characteristics (output voltage as a function of duty cycles *ZD* and *D*) is represented in Figure 14. In order to verify it, a specific area in the calculated gain characteristics was chosen (Figure 14, grey shadowed), and the calculated results were compared to the measured ones. Measured results are presented in Table 1, whereas comparison of measured and calculated values is shown in Figure 15a,b. When observing Figure 14 it shall be noted that it represents the calculated values, and, in the real operation the duty cycle *D* cannot be lower than *ZD*.

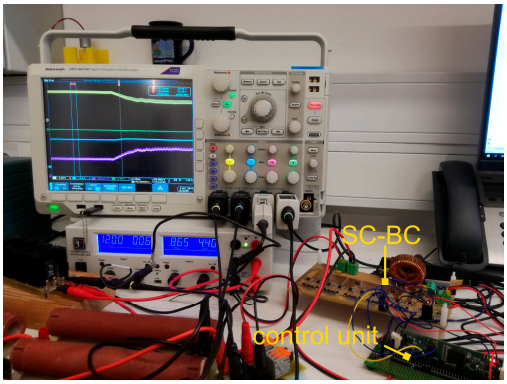

Figure 13. Experimental setup.

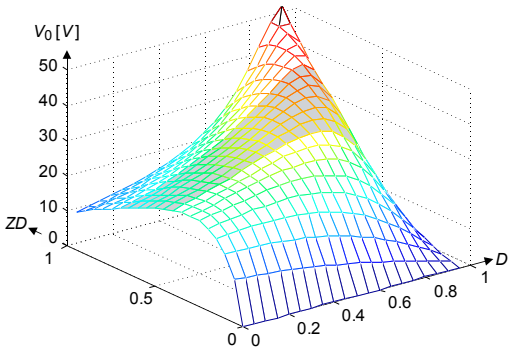

Figure 14. Calculated output voltage V_0 of SC-BC—static characteristics (function of ZD and D); shaded area is used for verification purposes.

Table 1. Measurement results.

	ZD = 0.4	ZD = 0.5
D	V_0 (V)	V_0 (V)
0.40	24.00	-
0.50	25.90	24.90
0.60	27.47	26.93
0.70	27.75	28.20
0.80	25.10	26.55
0.90	17.82	19.60

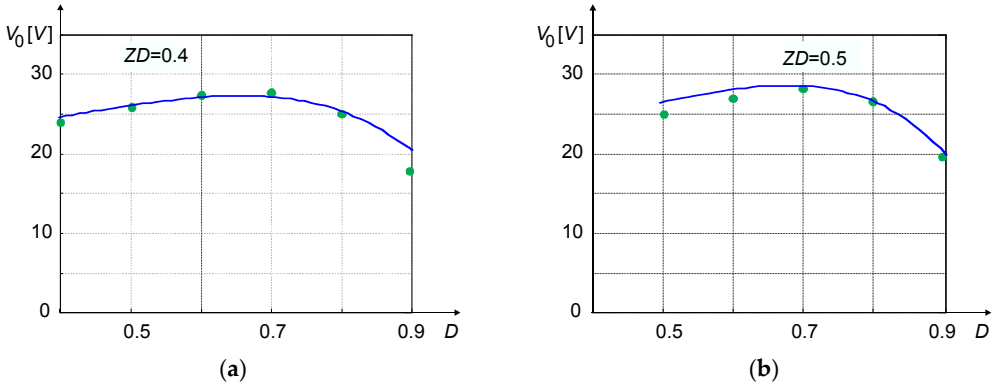

Figure 15. Static characteristics of output voltage V_0; green dots (measured) and blue curve (calculated): (**a**) $V_0 = f(D)$ when $ZD = 0.4$; (**b**) $V_0 = f(D)$ when $ZD = 0.5$.

For measurement verification the control variable ZD was chosen as $ZD = 0.4$, and $ZD = 0.5$, respectively, and for every chosen ZD, the control variable D was changed within the area $D \in (0.4, 0.9)$. It is important to note that in the real operation the value of duty cycle D can only be higher than ZD, because Z can only be lower than or equal to 1. Duty cycle D is also limited to the maximal value, as was determined in Equation (22), and is approximately at $D = 0.7$. In the simulations and experimentation, from which the results in the following text were obtained, Equation (22) was used for the on-line calculation of the D upper limit. As a result of this limitation the available range of output voltage is also limited. Based on the measurement results collected in Table 1, the maximal distance between measurement points and theoretical calculated curve (represented as performance index ε), was evaluated as $\varepsilon = \pm 2.5\%$. The measurement points are indicated by green dots, and theoretical calculated curves are drawn in blue, and are shown in Figure 15a,b. According to the thermal properties of inner and output resistance (R_g and R_0), the gain analysis performed in Section 4 is sufficiently precise for further study, for example, for study and introduction of the Maximum Power Point Tracking (MPPT) algorithms. According to the theoretical calculation and measurement, it can be concluded that the developed gain model gives representative results.

7.2. Control Algorithm Verification, Simulation and Experimentation

In order to evaluate the behaviour of the control algorithm, simulations and experiments were performed for the inductor current and output voltage control. MATLAB/Simulink was used for the simulations, specifically the SimPowerSystems Toolbox. The discrete time control was applied to emulate the behaviour in the case of the experiments. The system model used in simulations applied the realistic parameters of the converter. As was proven by results in the following text, the simulation model resembles the operation of the real SC-BC DC-DC converter adequately. In experimentation, the control algorithm was implemented using a digital signal controller, TMS320F28335 by Texas Instruments (Dallas, TX, USA), programmed using the MATLAB/Simulink Embedded Coder (for Texas Instruments C2000 microcontrollers). Both simulations and experimentation were first performed for the control of inductor current i_L, and then for the output voltage v_0. In the case of output voltage control, the inductor current control was used as the inner control loop, as represented in Figure 11.

It is important to note that the operation of the SC-BC is limited regarding the range of both inductor current and output voltage. The limitations are due to the boost converter operation, where the output voltage value cannot be below the input voltage value, whereas the static characteristics (Figure 15) limit the maximal value of the output voltage. This behaviour is also reflected in the available range of inductor current, where the minimal and maximal values also limit the operation. The converter is strictly unidirectional. The behaviour regarding the limits is dependent on the set value of the ZD.

7.2.1. Inductor Current Control

The current control was first investigated with the simulations and, later, with the experimentation. During the current control, the whole system was organised as a current source to support the PV DC voltage. The output current I_{R0} (current through the load R_0) was controlled implicitly by controlling the inductor current, so the full attention was concentrated to the inductor current control. Figure 16 shows the simulation results, and Figure 17 the experimental results when $ZD = 40\%$, output resistance was $R_0 = 70\ \Omega$, and TEG open terminal voltage was $V_g = 8.65$ V. For the simulation results in Figure 16, the top graph shows the output voltage v_0 and converter input voltage (TEG output voltage) v_{gg}. The output voltage v_0 is represented in red, and the converter input voltage v_{gg} in blue. On the bottom graph, the inductor current is represented, the reference value I_L^d in blue and the actual value i_L in green. The same presentation (top and bottom graphs) and colour scheme are used for the representation of the same values in the case of the experimental results shown in Figure 17, with the exception of I_L^d, which is represented in black.

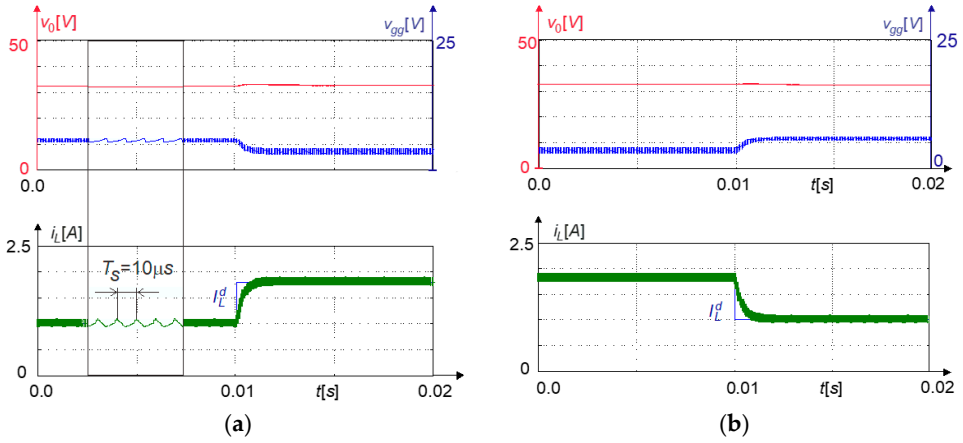

Figure 16. Simulation results, current control, transients when ZD = 40%, R_0 = 70 Ω and reference current changes: (**a**) From 1.0 A to 1.8 A; (**b**) From 1.8 A to 1.0 A.

A precise tracking of the inductor current is presented in both cases, in simulations and experiments. In the case of the increased reference value of the inductor current i_L, the input current demand was also increased, thereby reducing the value of the converter input voltage v_{gg}, due to the voltage drop on the TEG inner resistance R_g. To represent the behaviour of the converter better, the cut-out of the voltages and currents is represented, showing the behaviour of the variables in the smaller time measure. The behaviour as represented in Figure 4b can be observed for the inductor current in the cut-out for both simulations and experimental results. The input voltage of SC-BC was proven to exhibit only a moderate ripple. At this point, it is important to note that the resistances of capacitors and MOSFETs were not considered in the control design process, and the TEG internal resistance was not known with a very high precision. Thus, the stable operation in the case of experimental results also proves the robustness of the control to the variations of R_g.

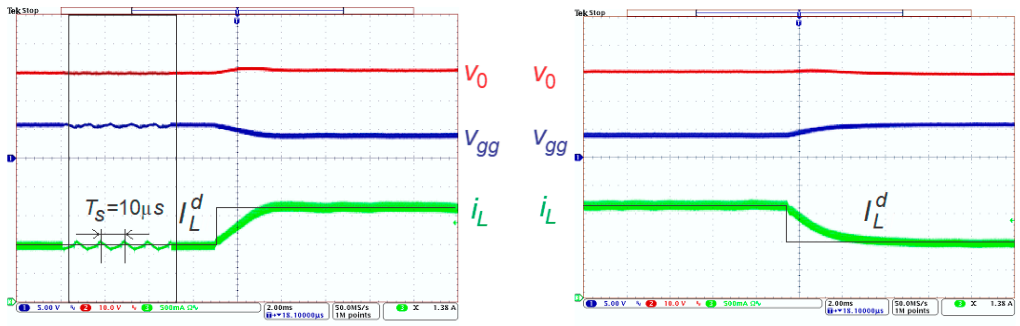

Figure 17. Experimental results, current control, transients when ZD = 40%, R_0 = 80 Ω and reference current changes: (**a**) From 1.0 A to 1.8 A; (**b**) From 1.8 A to 1.0 A; x-axis 2 ms/div, y-axis; v_0-10 V/div, v_{gg}-5 V/div, i_L-500 mA/div.

The operation under the changing load condition is represented in Figures 18 and 19, when ZD = 40% and current reference was set to I_L^d = 1.2 A. TEG open terminal voltage was again V_g = 8.65 V. Figure 18 features the simulation results, and the experimental results are presented in Figure 19. Transients in the case of output resistance R_0 changing from 60 Ω to 80 Ω are represented in Figures 18 and 19, whereas Figures 18 and 19 represent the behaviour in the case when the output resistance R_0 changed from 80 Ω to 60 Ω. Again, for both simulation and experimental results, the top graph shows the output voltage v_0 and converter input voltage (TEG output voltage) v_{gg}, where the output voltage is represented in red and the converter input voltage in blue. The bottom graph shows

the inductor current, where the reference value I_L^d is shown in blue (in black for the experimental results) and the actual value i_L in green.

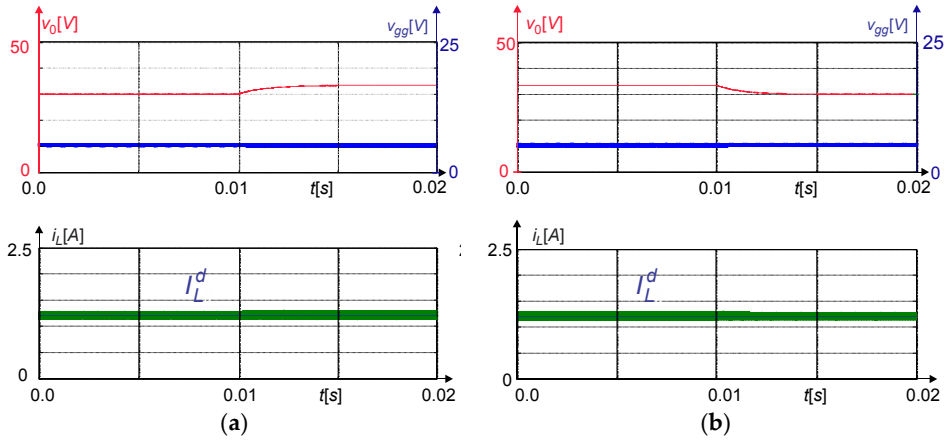

Figure 18. Simulation results, current control, ZD = 40% and current reference is set to I_L^d = 1.2 A, transients when output resistance R_0 was changed from: (**a**) 60 Ω to 80 Ω; (**b**) 80 Ω to 60 Ω.

A good rejection of the load variation can be observed, and the value of the inductor current remains almost unchanged. As expected, the converter input voltage remains unchanged, whereas the output voltage is increased in the case of reduced load (higher load resistance), and reduced in the case of higher load (smaller load resistance). As expected, the variation of the load resistance has no impact on the control stability. From the simulation and experimental results it can be observed that the load variation rejection is completed in about 1ms. In the case of the simulation results, the inductor current does not vary significantly, but the transient can be observed in the output voltage. In the experimental results, the current transient can be observed, but it is within the range of 10% of the set value. The transient is a result of both load variation and the impact of the TEG parameter variations from the estimated values.

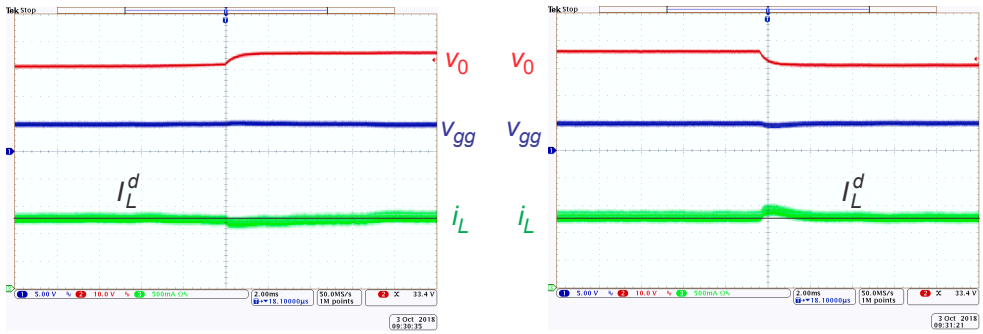

Figure 19. Experimental results, current control, ZD = 40% and current reference is set to I_L^d = 1.2 A, transients when output resistance R_0 was changed from: (**a**) 60 Ω to 80 Ω; (**b**) 80 Ω to 60 Ω; where x-axis 2 ms/div, y-axis; v_0-10 V/div, v_{gg}-5 V/div, i_L-500 mA/div.

The operation of the SC-BC is also demonstrated in Figures 20–23 for the case when the ZD was set to a higher value (ZD = 50%). Simulation results are presented in Figure 20 and experimental results in Figure 21 for the changing desired value of the inductor current (from 1.4 A to 2.0 A and from 1.8 A to 1.0 A, when R_0 = 60 Ω, V_g = 8.65 V), whereas the behaviour under changing load (R_0 changed from 60 Ω to 80 Ω and from 80 Ω to 60 Ω, when I_L^d = 1.5 A) is shown in Figures 22 and 23. As was the case in the results for the lower value of product ZD (ZD = 40%), for both simulation and

experimental results, the top graph shows the output voltage v_0 and converter input voltage (TEG output voltage) v_{gg}.

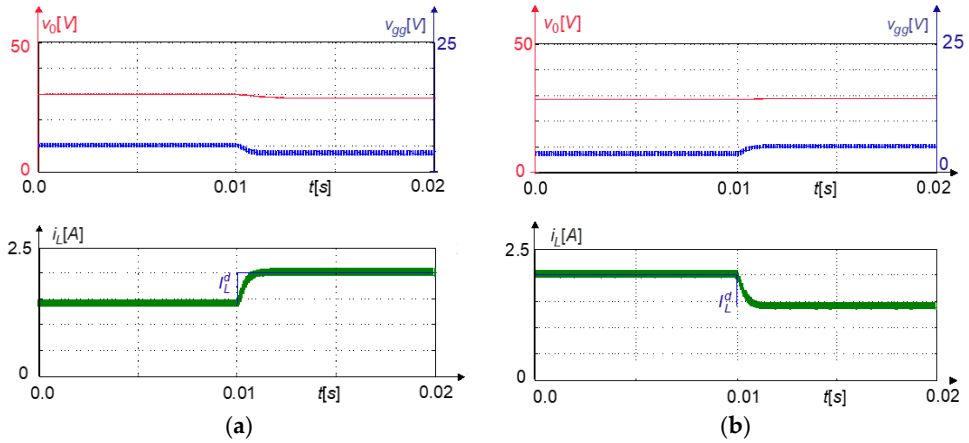

Figure 20. Simulation results, current control, transients when ZD = 50%, R_0 = 70 Ω and reference current changes from: (**a**) 1.4 A to 2.0 A; (**b**) 1.8 A to 1.0 A.

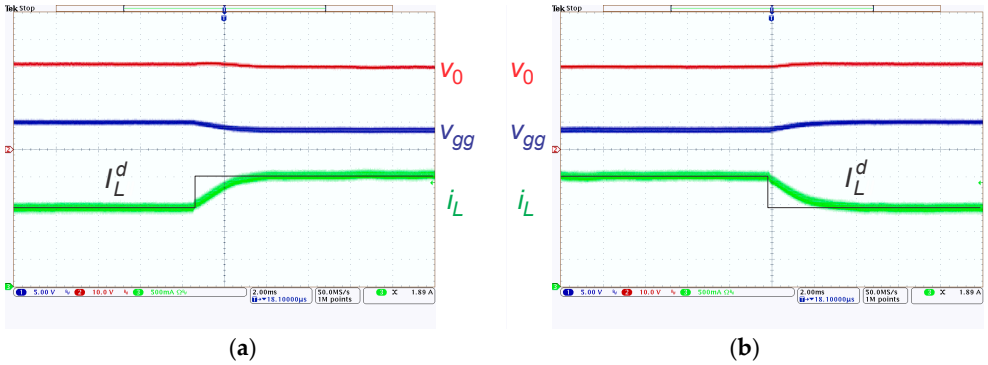

Figure 21. Experimental results, current control, transients when ZD = 50%, R_0 = 60 Ω and reference current changes from: (**a**) 1.4 A to 2.0 A; (**b**) 1.8 A to 1.0 A; where x-axis 2 ms/div, y-axis; v_0-10 V/div, v_{gg}-5 V/div, i_L-500 mA/div.

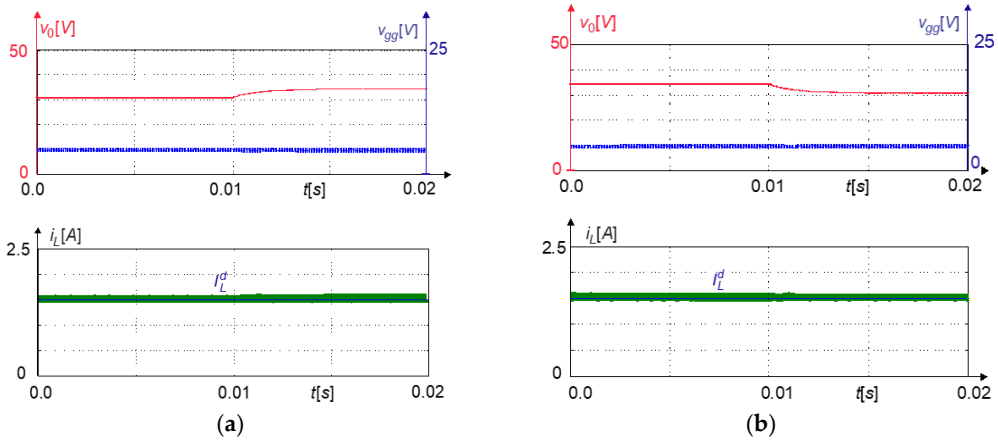

Figure 22. Simulation results, current control, ZD = 50% and current reference is set to I_L^d = 1.5 A, transients when output resistance R_0 was changed from: (**a**) 70 Ω to 80 Ω; (**b**) 80 Ω to 70 Ω.

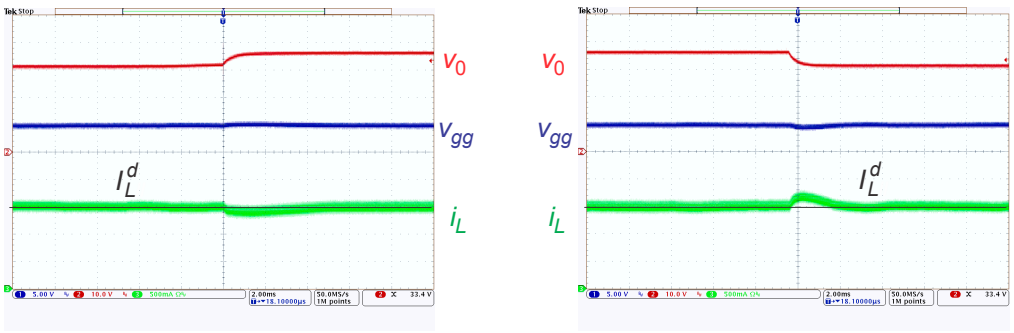

(**a**) (**b**)

Figure 23. Experimental results, current control, ZD = 50% and current reference is set to I_L^d = 1.5 A, transients when output resistance R_0 was changed from: (**a**) 70 Ω to 80 Ω; (**b**) 80 Ω to 70 Ω; where x-axis 2 ms/div, y-axis; v_0-10V/div, v_{gg}-5 V/div, i_L-500 mA/div.

The output voltage is represented in red and the converter input voltage in blue. The bottom graphs show the inductor current, where the reference value I_L^d is shown in blue (in black for the experimental results) and the actual value i_L in green. It can be observed from both simulation and experimental results that the precise tracking of the reference value has also been achieved for the ZD = 50%, and also the impact of load variation was compensated for successfully.

If the results from Figures 20–23 are compared to the ones from the Figures 16–19, it can be observed that the control behaviour remains similar, and the transient times are not changed significantly. Because in most cases of practical use of SC-BC the value of ZD will be set to the values in the range of about 0.4 to 0.5, this represents a stable and robust operation in the working range of SC-BC. Higher values of ZD would not be practical, because the available range of D is up to the value of approximately 0.7, as represented in Figures 14 and 15, as well as Equation (22).

7.2.2. Output Voltage Control

Output voltage control was, as was the case for the current control, demonstrated with the simulations and experiments. Operation with changing reference value of the output voltage is presented in Figure 24 (simulation results) and Figure 25 (experimental results). In Figure 24a, the performance when voltage reference V_0^d was increased from 32 V to 35 V is represented, whereas in Figure 24b, the case when the output voltage reference was reduced from 35 V to 30 V is shown. In Figure 25a the transients when voltage reference V_0^d was changing from 30 V to 35 V, and in Figure 25 the voltage reference V_0^d was changing from 35 V to 30 V. The product ZD was set to the constant value (ZD = 40%), and the load resistance R_0 to 80 Ω. TEG open terminal voltage was V_g = 8.65 V.

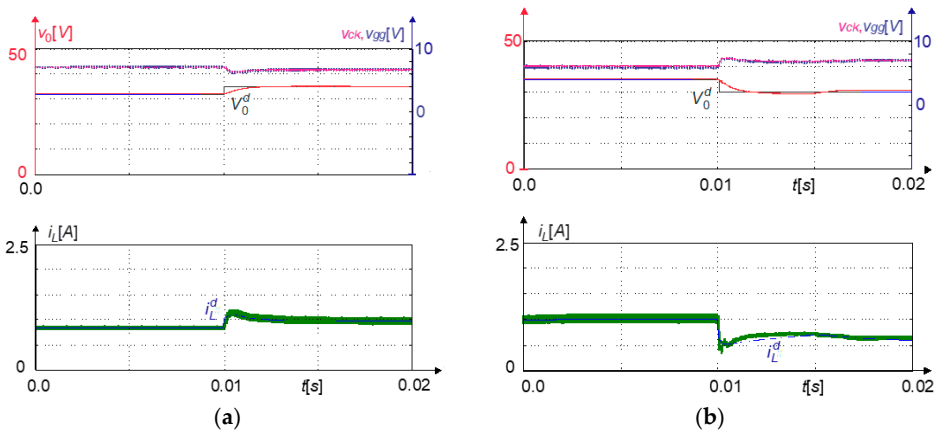

(**a**) (**b**)

Figure 24. Simulation results, voltage control when ZD = 40%, R_0 = 80 Ω and transients when voltage reference V_0^d was changing from: (**a**) 32 V to 35 V; (**b**) 35 V to 30 V.

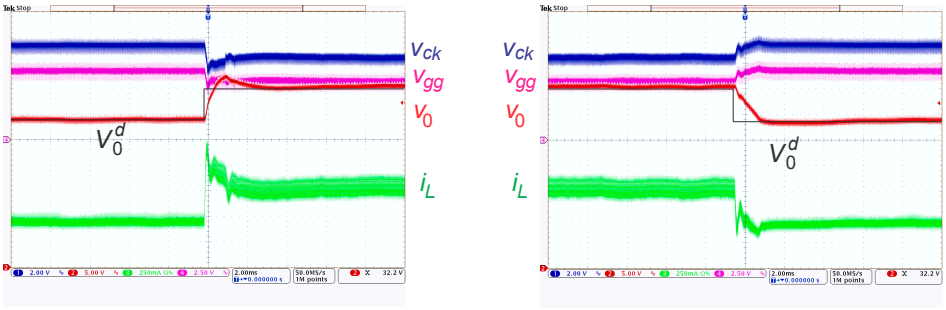

(**a**) (**b**)

Figure 25. Experimental results, voltage control when ZD = 40%, R_0 = 80 Ω and transients when voltage reference V_0^d was changing from: (**a**) 30 V to 35 V; (**b**) 35 V to 30 V; where x-axis 1 ms/div, y-axis; v_0-10 V/div, v_{gg}-5 V/div, v_{Ck}-5 V/div i_L-500 mA/div.

For both simulation and experimental results, the top graph shows the output voltage v_0 (represented in red), its reference value V_0^d (represented in black), the voltage on the SC stage capacitors v_{Ck} (represented in pink), and converter input voltage (TEG output voltage) v_{gg} (represented in blue). On the bottom graph for the simulation results, the inductor current is represented in green and its reference value I_L^d in black. The same presentation (top and bottom graphs) and colour scheme are used for the representation of the same values in the case of the experimental results, with the exception of the reference value of the inductor current, which cannot be represented for the experimental results. This representation, including the colour scheme, was also used in the additional experimental results featured in Figures 26–29.

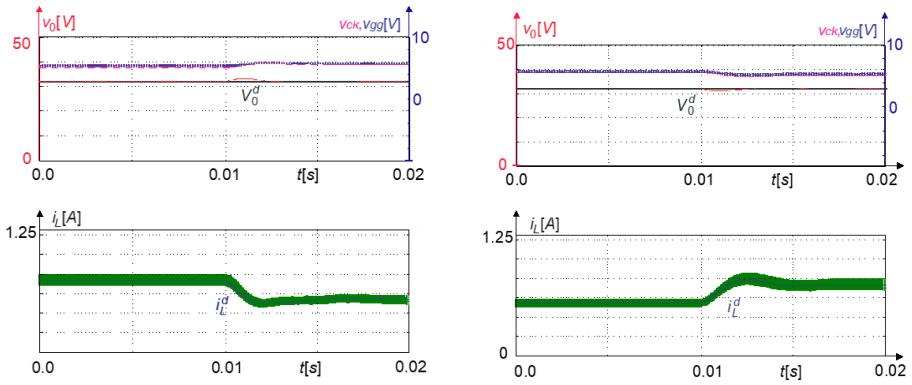

(**a**) (**b**)

Figure 26. Simulation results, voltage control when ZD = 40%, V_0^d = 32 V, transients when output resistance R_0 was changing from: (**a**) 100 Ω to 80 Ω; (**b**) 80 Ω to 100 Ω.

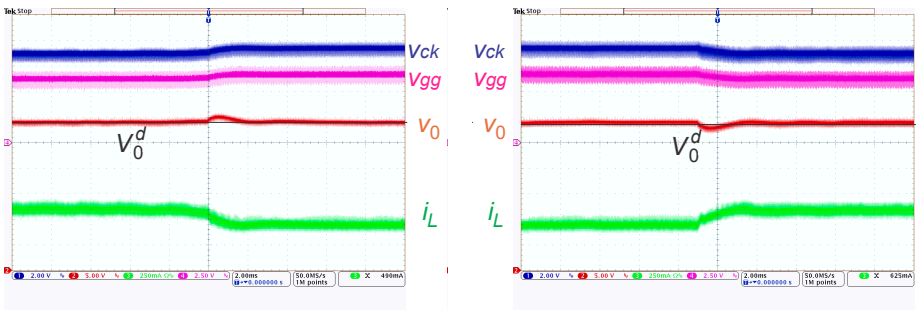

(**a**) (**b**)

Figure 27. Experimental results, voltage control when ZD = 40% and voltage reference was set to V_0^d = 30 V, transients when output resistance R_0 was changed from: (**a**) 80 Ω to 100 Ω; (**b**) 100 Ω to 80 Ω; where x-axis 1 ms/div, y-axis; v_0-5 V/div, v_{gg}-2.5 V/div, v_{Ck}-2 V/div i_L-250 mA/div.

Satisfactory output voltage tracking behaviour can be observed for both simulation and experimental results. The overshoot represented in experimental results for increased desired output voltage can be reduced with the appropriate choice of linear controller parameters. In the case of increased output voltage demand, the converter input voltage drops, together with the voltage on the capacitors in the SC-circuit. A good tracking behaviour can also be observed for the inductor current (controlled in the inner control loop). An overshoot can be observed in the inductor current response, as a result of the overshoot in the output voltage response.

The results show that the operation is not completely symmetrical in terms of the transient when the desired voltage value is increased or decreased. This is due to the fact that the SC-BC is strictly unidirectional, and the increased load demands can be covered for from the source (TEG), whereas in the case of load reduction, the excess energy can only be consumed by the load. This behaviour is evident in both the simulation and experimental results. It is also important to note that, as opposed to the inductor current control, the linearization method is not very precise, as it required for the use of several assumptions and approximations.

The behaviour in the case of the load variation for $ZD = 40\%$ is represented in Figure 26 (simulation results) and Figure 27 (experimental results). The reference value of the output voltage was 32 V (30 V for experimental results), and the output resistance R_0 was changing from 100 Ω to 80 Ω (Figures 26 and 27) 80 Ω to 100 Ω (Figures 26 and 27). It can be observed that the voltage controller rejects the effect of the load variation successfully in both cases. The transient is relatively fast, in the range of 3 ms, and the resulting overshoot is low, in the range of 2 V (at the output voltage set to 30 V this is between 5 and 10%). The current response also exhibits an overshoot; after the transient, the current settles at the higher value in the case of the increased load, and at the lower value in the case of the reduced load. The converter input voltage v_{gg} and the SC-circuit capacitance voltage v_{Ck} again show almost exact matching, as expected.

To prove the successful operation of the voltage controlled SC-BC further, additional experimental results are featured in Figures 28 and 29. Figure 28 features the case when the product ZD was set to the higher value ($ZD = 50\%$) and the voltage reference V_0^d was increased from 30 V to 35 V (Figure 28a) and decreased from 35 V to 30 V (Figure 28b). The load resistance R_0 is 80 Ω and TEG open terminal voltage was $V_g = 8.65$ V. A good output voltage tracking with a small overshoot in both output voltage and current can be observed.

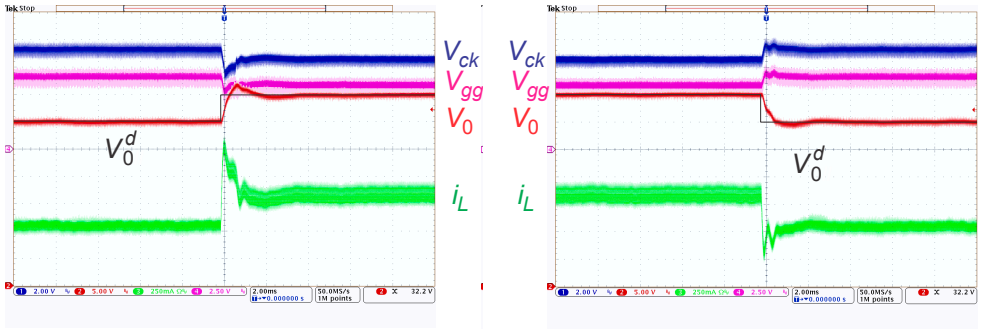

(**a**) (**b**)

Figure 28. Experimental results, voltage control when $ZD = 50\%$, $R_0 = 80$ Ω; transients when voltage reference V_0^d was changing from: (**a**) 30 V to 35 V; (**b**) 35 V to 30 V; where x-axis 1 ms/div, y-axis; v_0-5 V/div, v_{gg}-2.5 V/div, v_{Ck}-2 V/div i_L-250 mA/div.

To demonstrate the load variation rejection for the duty cycle product ZD set to 50% and the reference value of the output voltage set to 30 V, the experimental results are shown in Figure 29, for the cases when the output resistance R_0 was changed from 80 Ω to 100 Ω (Figure 29a) and from 100 Ω to 80 Ω (Figure 29b). After the short transient, the output voltage was kept on the same value it had before the changing of voltage, closely tracking the reference value. The output voltage overshoot

was in the range of 2 V with the duration of about 1 ms. The inductor current decreased in the case of the reduced load and increased in the case of increased load, as expected.

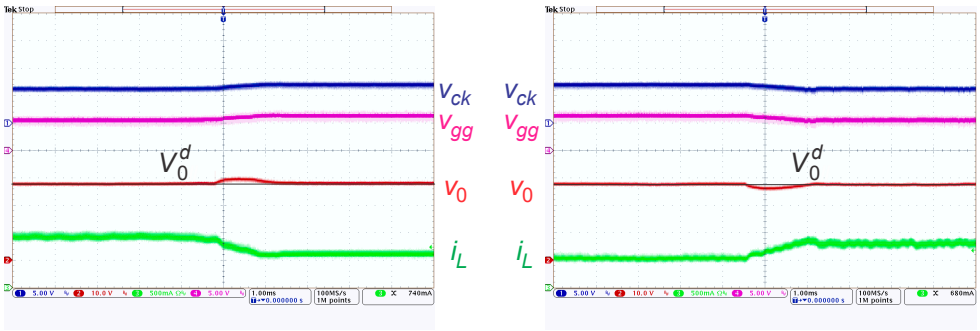

(**a**) (**b**)

Figure 29. Experimental results, voltage control when ZD = 50% and voltage reference was set to V_0^d = 30 V, transients when output resistance R_0 was changed from: (**a**) 80 Ω to 100 Ω; (**b**) 100 Ω to 80 Ω; where x-axis 2 ms/div, y-axis; v_0-5 V/div, v_{gg}-2.5 V/div, v_{Ck}-2 V/div i_L-250 mA/div.

Like in the case of the inductor current control, the value of ZD was set to the values 0.4 and 0.5, and the maximal value of D was set to approximately 0.7, as calculated using Equation (22). Thus, again, the performance was represented in the complete operation area. The behaviour of the SC-BC was only shown with the experimental results for ZD = 0.5, because the results do not differ significantly from the ones obtained for ZD = 0.4, which is demonstrated sufficiently with the experimental results.

The stable operation of the control algorithms can be demonstrated with the use of the simulation and experimental results. Within the available limits of the operation, the SC-BC operation was shown to be satisfactory.

8. Discussion

A switched-capacitor boost DC-DC converter to be applied for thermal energy harvesting in PV systems is presented in this paper. When such a converter is applied, additional energy can be obtained from the PV panels, increasing their performance and cost effectiveness. TEGs, placed on the backside of the panel, can be used for the input of the converter, and, in a typical application, the converter is connected in parallel with the main PV converter, operating as a current source. In this case, only current control is required, and, because the value of the converter output current can be calculated easily using the static characteristics of the converter, the control of the inductor current would be sufficient. However, the output voltage control was also developed and evaluated to represent the possibility of a standalone operation and evaluate the full potential of the converter.

The converter is an integration of the switched-capacitor circuit and a boost converter. It can be used in applications where no galvanic isolation is required. The MOSFETs were used as switching elements rather than diodes, because their conducting power losses are lower, and the voltage drop on the MOSFET is significantly lower than the diode forward voltage drop. It has been demonstrated by analytical studies, as well as simulations and experiments, that a voltage gain can be increased significantly, which is of special importance in the case of using TEGs, where the output voltage is relatively low. The efficiency was increased significantly. In the optimal point (Z = 0.8, D = 0.6) the efficiency of 95% was reached, whereas with the use of the diode based converter with the same power rating and passive elements' values, the maximal efficiency achieved was 79%. The voltage could be increased to achieve an even higher voltage gain by simply adding more capacitor stages in the SC. The converter can operate with relatively low duty cycles.

Additionally, if compared to the other recently published methods, the number of inductors is low, and the MOSFETs used as switches can be integrated. In case of very low power this can also be true for SC capacitors. The values of passive components, BC inductance L, as well as output BC

capacitance C_0 and SC capacitance C_k, were calculated, and the method of their choice is presented in the paper. Likewise, the limitations of the operating parameters (duty cycle D) of the converter were evaluated and used for the on-line setting of controller limits.

The dynamics of the converter were evaluated, and a dynamic model was created using the state-averaging method. The behaviour of not only inductor current and output voltage, but also the capacitor voltage and current in the switched capacitors' stage, can be evaluated with the use of this model. Also, the control algorithms for inductor current and output voltage were developed based on this model. Linearization methods were used. The linearised models were controlled by classical linear PI controllers. The dynamics of the converter are highly nonlinear, and the use of only linear controllers would not be sufficient for stable and robust control behaviour. The model-based approach is applied for the linearization, utilising the model obtained by the state space averaging method. This approach enables the operation in a relatively wide area, not only in a single operating point.

The effects of the variation of SC-BC parameters were evaluated, as well as the varying load. It was shown that the control algorithm is not significantly impacted by the parameter mismatches, and the control behaviour remains stable.

To summarise, the main advantages of the SC-BC presented in the paper are:

- Only one inductor is used and no transformers,
- MOSFETs are used in place of diodes as switching elements, resulting in low conduction losses,
- Duty cycles are not overlong,
- The switching-capacitor stage can be integrated.

On the other hand, in our view, the main disadvantages are the number of switching elements and relatively complex control. The high number of switches can be overcome by the integration, whereas the complex control is becoming an ever smaller problem due to the rapid advance in integrated circuits, microcontrollers and SOCs.

Simulation and experimental results for the 30 W DC-DC converter are included, which verify the proposed converter structure and control approach. In both cases, satisfactory results can be observed regarding the response to the changed desired value of inductor current and output voltage, as well as the varying load.

In future work, the focus will be on the simplification of the control algorithm and extending the operation range by control of the switched capacitor voltage. Robustness to the TEG parameter variations will remain an important issue. MPPT algorithms will be developed for the determination of the most appropriate value of switched capacitors' charging duty cycle z. Using a different, possibly integral, method for the measurement of currents will also be of interest.

Author Contributions: All authors contributed equally to the paper. They developed the converter and control algorithms jointly. They also performed experiments and evaluated results jointly.

Funding: This research received no external funding.

Conflicts of Interest: The authors declare no conflict of interest.

Abbreviations

Acronyms

BS	Boost Stage
CCM	Continuous Conduction Mode
DC	Direct Current
DC-DC	Direct Current-Direct Current
DCM	Discontinuous Conduction Mode
ESR	Equivalent Series Resistance of capacitor
MOSFET	Metal-Oxide-Semiconductor Field-Effect Transistor
MPPT	Maximum Power Point Tracking

PI	Proportional-Integral
PV	Photovoltaic
PWM	Pulse Width Modulation
SC	Switched-Capacitor
SC-BC	Switched-Capacitor-Boost Converter
SOC	System On Chip
TEG	Thermoelectric generator

Nomenclature

A_v	converter static gain
C_0	output capacitance
C_1, C_2, C_3	capacitances of switched capacitors
C_k	capacitance of switched capacitors
d	duty-cycle function over the interval T_s
D	average value of duty-cycle function over the interval T_s
D_{max}	maximal value of duty cycle
D_{min}	minimal value of duty cycle
f_s	switching frequency of the converter
i_{in}	converter input current
I_{in}	average value of converter input current over the interval T_s
i_L	inductor current
I_L	average value of inductor current $\mathrm{i_L}$ over the interval T_s
$I_L(s)$	Laplace transform of I_L
i_L^d	desired value of inductor current
I_L^d	average value of desired value of inductor current over the interval T_s
$I_L^d(s)$	Laplace transform of i_L^d
$I_{L,max}$	maximal value of inductor current (current ripple)
$I_{L,min}$	minimal value of inductor current (current ripple)
i_{R0}	output current
I_{R0}	average value of output current $\mathrm{i_{R0}}$ over the interval T_s
$I_{R0}(s)$	Laplace transform of I_{R0}
L	inductance of the boost stage inductor
R_0	output (load) resistance
$r_{d1} - r_{d6}$	MOSFET drain-source on resistance of transistors $T_{1d} - T_{6d}$
$r_{ds1} - r_{ds5}$	MOSFET drain-source on resistance of transistors $T_1 - T_5$
$R_{DS(on)}$	MOSFET drain-source on resistance
R_g	inner TEG resistance
R_L	resistance of the boost stage inductor
t	time
T_s	sample time interval
u_{iL}	linear feedback inductor current controller output
U_{iL}	average value of linear feedback inductor current controller output over the interval T_s
$U_{iL}(s)$	Laplace transform of U_{iL}
u_{v0}	linear feedback output voltage controller output
U_{v0}	average value of linear feedback output voltage controller output over the interval T_s
$U_{v0}(s)$	Laplace transform of U_{v0}
u_{vCk}	linear feedback switched capacitor voltage controller output
U_{vCk}	average value of linear feedback switched capacitor voltage controller output over the interval T_s
$U_{vCk}(s)$	Laplace transform of U_{vCk}
v_0	output voltage
V_0	average value of output voltage over the interval T_s
$V_0(s)$	Laplace transform of V_0
v_0^d	desired value of the output voltage
V_0^d	average value of desired value of the output voltage over the interval T_s
$V_0^d(s)$	Laplace transform of V_0^d

$v_{0,max}$	maximal value of output voltage (voltage ripple)
$v_{0,min}$	minimal value of output voltage (voltage ripple)
v_{Ck}	switched capacitor voltage
V_{Ck}	average value of switched capacitor voltage over the interval T_s
$V_{Ck}(s)$	Laplace transform of V_{Ck}
v_{Ck}^d	desired value of the switched capacitor voltage
V_{Ck}^d	average value of desired value of the switched capacitor voltage over the interval T_s
$V_{Ck}^d(s)$	Laplace transform of V_{Ck}^d
V_D	diode forward voltage
v_g	open terminal TEG voltage
V_g	average value of open terminal TEG voltage over the interval T_s
v_{gg}	SC_BC input terminal voltage
V_{gg}	SC_BC input terminal voltage over the interval T_s
V_{gg}^*	input of the boost stage of SC-BC, average value over the interval T_s
v_L	inductor voltage
W_L	energy stored in inductor L
W_{Ck}	energy stored in capacitor
z	switched capacitors charging duty cycle over the interval T_s
Z	average value of the switched capacitors charging duty cycle over the interval T_s
Δi_L	inductor current ripple
Δv_0	output voltage ripple
ε	maximal distance between measurement points and theoretical calculated curve

References

1. Chandrasekar, M.; Suresh, S.; Senthilkumar, T.; Ganesh Karthikeyan, M. Passive cooling of standalone flat PV module with cotton wick structures. *Energy Convers. Manag.* **2013**, *71*, 43–50. [CrossRef]
2. Wang, C.; Chen, W.; Shao, S.; Chen, Z.; Zhu, B.; Li, H. Energy management of standalone hybrid PV system. *Energy Procedia* **2011**, *12*, 471–479. [CrossRef]
3. Gentle, A.R.; Smith, G.B. Is enhanced radiative cooling of solar cell modules worth pursuing? *Sol. Energy Mater. Sol. Cells* **2016**, *150*, 39–42. [CrossRef]
4. Chandrasekar, M.; Senthilkumar, T. Passive thermal regulation of flat PV modules by coupling the mechanisms of evaporative and fin cooling. *Heat Mass Transf.* **2016**, *52*, 1381. [CrossRef]
5. Yang, D.; Yin, H. Energy Conversion Efficiency of a Novel Hybrid Solar System for Photovoltaic, Thermoelectric, and Heat Utilization. *IEEE Trans. Energy Convers.* **2011**, *26*, 662–670. [CrossRef]
6. Li, G.; Chen, X.; Jin, Y. Analysis of the Primary Constraint Conditions of an Efficient Photovoltaic-Thermoelectric Hybrid System. *Energies* **2017**, *10*, 20. [CrossRef]
7. Narducci, D.; Lorenzi, B. Challenges and perspectives in tandem thermoelectric-photovoltaic solar energy conversion. *IEEE Trans Nanotechnol.* **2016**, *15*, 348–355. [CrossRef]
8. Petucco, A.; Saggini, S.; Corradini, L.; Mattavelli, P. Analysis of power processing architectures for thermoelectric energy harvesting. *IEEE J. Emerg. Sel. Top. Power Electron.* **2016**, *4*, 1036–1049. [CrossRef]
9. Shen, C.-L.; Chen, H.-Y.; Chiu, P.-C. Integrated Three-Voltage-Booster DC-DC Converter to Achieve High Voltage Gain with Leakage-Energy Recycling for PV or Fuel-Cell Power Systems. *Energies* **2015**, *8*, 9843–9859. [CrossRef]
10. Wong, Y.-S.; Chen, J.-F.; Liu, K.-B.; Hsieh, Y.-P. A Novel High Step-Up DC-DC Converter with Coupled Inductor and Switched Clamp Capacitor Techniques for Photovoltaic Systems. *Energies* **2017**, *10*, 378. [CrossRef]
11. Shen, C.-L.; Chiu, P.-C.; Lee, Y.-C. Novel Interleaved Converter with Extra-High Voltage Gain to Process Low-Voltage Renewable-Energy Generation. *Energies* **2016**, *9*, 871. [CrossRef]
12. Leon-Masich, A.; Valderrama-Blavi, H.; Bosque-Moncusí, J.M.; Maixé-Altés, J.; Martínez-Salamero, L. Sliding-Mode-Control-Based Boost Converter for High-Voltage–Low-Power Applications. *IEEE Trans. Ind. Electron.* **2015**, *62*, 229–237. [CrossRef]
13. Luo, F.L.; Ye, H. *Advanced DC/DC Converters*, 2nd ed.; CRC Press: Boca Raton, FL, USA, 2017; ISBN 978-1498774901.
14. Luo, F.L.; Ye, H. Super-lift boost converters. *IET Power Electron.* **2014**, *7*, 1655–1664. [CrossRef]

15. Ioinovici, A. Switched-capacitor power electronics circuits. *IEEE Circuits Syst. Mag.* **2001**, *1*, 37–42. [CrossRef]
16. Wu, B.; Li, S.; Smedley, K.M.; Singer, S. Analysis of highpower switched capacitor converter regulation based on charge-balance transient-calculation method. *IEEE Trans. Power Electron.* **2016**, *31*, 3482–3494. [CrossRef]
17. Maksimovic, D.; Ćuk, S. Switching converters with wide DC conversion range. *IEEE Trans. Power Electron.* **1991**, *6*, 151–157. [CrossRef]
18. Wijeratne, D.S.; Moschopoulos, G. Quadratic Power Conversion for Power Electronics: Principles and Circuits. *IEEE Trans. Circuits Syst. Regul. Pap.* **2012**, *59*, 426–438. [CrossRef]
19. Loera-Palomo, R.; Morales-Saldana, J.A. Family of quadratic step-up dc–dc converters based on non-cascading structures. *IET Power Electron.* **2015**, *8*, 793–801. [CrossRef]
20. Divya Navamani, J.; Vijayakumar, K.; Jegatheesan, R. Non-isolated high gain DC-DC converter by quadratic boost converter and voltage multiplier cell. *Ain Shams Eng. J.* **2016**. [CrossRef]
21. Axelrod, B.; Berkovich, Y.; Ioinovici, A. Switched-Capacitor/Switched-Inductor Structures for Getting Transformerless Hybrid DC–DC PWM Converters. *IEEE Trans. Circuits Syst. Regul. Pap.* **2008**, *55*, 687–696. [CrossRef]
22. Tran, V.-T.; Nguyen, M.-K.; Choi, Y.-O.; Cho, G.-B. Switched-Capacitor-Based High Boost DC-DC Converter. *Energies* **2018**, *11*, 987. [CrossRef]
23. Nguyen, M.; Duong, T.; Lim, Y. Switched-Capacitor-Based Dual-Switch High-Boost DC–DC Converter. *IEEE Trans. Power Electron.* **2018**, *33*, 4181–4189. [CrossRef]
24. Padmanaban, S.; Bhaskar, M.S.; Maroti, P.K.; Blaabjerg, F.; Fedák, V. An Original Transformer and Switched-Capacitor (T & SC)-Based Extension for DC-DC Boost Converter for High-Voltage/Low-Current Renewable Energy Applications: Hardware Implementation of a New T & SC Boost Converter. *Energies* **2018**, *11*, 783. [CrossRef]
25. Chen, S.-J.; Yang, S.-P.; Huang, C.-M.; Chou, H.-M.; Shen, M.-J. Interleaved High Step-Up DC-DC Converter Based on Voltage Multiplier Cell and Voltage-Stacking Techniques for Renewable Energy Applications. *Energies* **2018**, *11*, 1632. [CrossRef]
26. Abutbul, A.; Gherlitz, A.Y.; Berkovich, Y.; Ioinovici, A. Step-Up Switching-Mode Converter With High Voltage Gain Using a Switched-Capacitor Circuit. *IEEE Trans. Circuits Syst. I Fundam. Theory Appl.* **2003**, *50*, 1098–1102. [CrossRef]
27. Maruša, L.; Milanovič, M.; Valderrama-Blavi, H. Evaluating a Switched Capacitor-Boost Converter (SC-BC) for energy harvesting in a Peltier-cells thermoelectric system. In Proceedings of the Electrical Drives and Power Electronics Conference (EDPE), Tatranska Lomnica, Slovakia, 21–23 September 2015. [CrossRef]
28. Slotine, J.J.E.; Li, W. *Applied Nonlinear Control*; Prantice-Hall: Englewood Cliffs, NJ, USA, 1991; ISBN 978-0130408907.
29. Dodds, S.J. *Feedback Control*; Advanced Textbooks in Control and Signal Processing; Springer: London, UK, 2015; ISBN 978-1-4471-6674-0. [CrossRef]
30. Mohan, N.; Undeland, T.M.; Robbins, W.P. *Power Electronics: Converter, Application and Design*, 3rd ed.; John Wiley & Sons: New York, NY, USA, 2007; ISBN 978-8126510900.